Review

Small Molecular NIR-II Fluorophores for Cancer Phototheranostics
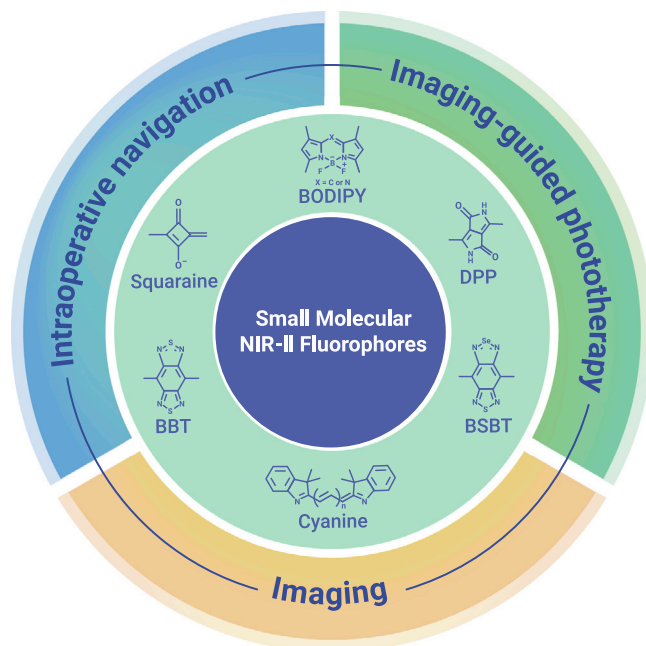
Hanming Dai,[1] Qing Shen,[1] Jinjun Shao,[1,*] Wenjun Wang,[2] Fan Gao,[3,*] and Xiaochen Dong[1,3,*]

*Correspondence: iamjjshao@njtech.edu.cn (J.S.); 003335@nuist.edu.cn (F.G.); iamxcdong@njtech.edu.cn (X.D.)

GRAPHICAL ABSTRACT

PUBLIC SUMMARY

- Phototheranostics combines diagnostic imaging with phototherapy, showing broad applications in the early diagnosis and precise treatment of tumors

- Small molecular NIR-II fluorophores with good biocompatibility, tunable structure, high imaging quality, and excellent phototoxicity, have shown great potential for cancer phototheranostics

- Small molecular NIR-II fluorophores with different central cores for cancer phototheranostics are summarized, highlighting the design strategies and phototheranostic performances

- Challenges and prospects of future development toward clinical translation are discussed

Small Molecular NIR-II Fluorophores for Cancer Phototheranostics

Hanming Dai,[1] Qing Shen,[1] Jinjun Shao,[1,*] Wenjun Wang,[2] Fan Gao,[3,*] and Xiaochen Dong[1,3,*]

[1]Key Laboratory of Flexible Electronics (KLOFE) and Institute of Advanced Materials (IAM), Nanjing Tech University (NanjingTech), Nanjing 211816, China
[2]School of Physical Science and Information Technology, Liaocheng University, Liaocheng 252059, China
[3]School of Chemistry and Materials Science, Nanjing University of Information Science & Technology, Nanjing 210044, China
*Correspondence: iamjjshao@njtech.edu.cn (J.S.); 003335@nuist.edu.cn (F.G.); iamxcdong@njtech.edu.cn (X.D.)

Citation: Hanming D., Qing S., Jinjun S., et al. (2021). Small molecular NIR-II fluorophores for cancer phototheranostics. The Innovation 2(1), 100082.

Phototheranostics integrates deep-tissue imaging with phototherapy (containing photothermal therapy and photodynamic therapy), holding great promise in early diagnosis and precision treatment of cancers. Recently, second near-infrared (NIR-II) fluorescence imaging exhibits the merits of high accuracy and specificity, as well as real-time detection. Among the NIR-II fluorophores, organic small molecular fluorophores have shown superior properties in the biocompatibility, variable structure, and tunable emission wavelength than the inorganic NIR-II materials. What's more, some small molecular fluorophores also display excellent cytotoxicity when illuminated with the NIR laser. This review summarizes the progress of small molecular NIR-II fluorophores with different central cores for cancer phototheranostics in the past few years, focusing on the molecular structures and phototheranostic performances. Furthermore, challenges and prospects of future development toward clinical translation are discussed.

KEYWORDS: second near-infrared (NIR-II); small molecular fluorophores; cancer phototheranostics

INTRODUCTION

Phototheranostics, which combines diagnostic photo-imaging with light-triggered precision therapy, can simultaneously locate the lesion sites and monitor the therapeutic effects in real time.[1–3] Thus, to achieve efficient and controllable precision treatment, it is necessary to integrate diagnostics with therapeutics.[4] Traditional diagnostic modalities, such as computed tomography (CT),[5–7] magnetic resonance imaging (MRI),[8–10] and positron emission tomography (PET),[11–13] face the problems of insufficient sensitivity, low resolution, poor signal-to-background ratio (SBR) and high cost.[14,15] As an emerging imaging modality, fluorescence imaging (FLI) has aroused extensive research enthusiasm due to its high sensitivity and excellent specificity.[16–18]

The FLI window can be divided into the visible region (400−700 nm), the first near-infrared region (NIR-I, 700−1,000 nm), and the second near-infrared region (NIR-II, 1,000−1,700 nm).[19] Though NIR-I FLI has better performance than visible light imaging; shallow tissue penetration hinders its further clinical applications.[20] By comparison, NIR-II FLI presents the superiority of high temporal and spatial resolution, excellent signal-to-noise ratio, and deep tissue penetration owing to the reduced tissue absorption and scattering as well as low autofluorescence.[21–23] In 2019, NIR-II FLI was reported for the first time to guide the surgery of liver cancer patients. The intraoperative evaluations confirmed that NIR-II FLI presented higher sensitivity and better lesion recognition ability compared with imaging in visible and NIR-I areas, which opened a new era of the cancer diagnosis.[24] At present, cancer treatment strategies, such as surgery,[25] radiotherapy,[26] and chemotherapy,[27] have certain side effects on the human body, which limit their therapeutic effects.[28] To achieve efficient, accurate, and noninvasive treatment, a series of diagnosis and treatment-integrated NIR-II fluorophores have been further developed for imaging-mediated phototherapy.[29–32] In the process of imaging-guided photothermal therapy (PTT), NIR-II fluorophores not only have

excellent diagnostic capabilities but also exhibit good photothermal conversion efficiency, which can convert light energy into heat to ablate tumors. Meanwhile, as-produced heat can cause thermal expansion of the tumor tissues to generate photoacoustic imaging (PAI) signal.[33–35] Furthermore, some NIR-II fluorophores can also produce singlet oxygen ($^1O_2$) or other reactive oxygen species (ROS) under laser irradiation to induce apoptosis or necrosis of tumor cells, which can be applied for imaging-guided photodynamic therapy (PDT) or further to achieve synergistic PDT/PTT.[36–40] These high-performance phototheranostic NIR-II fluorophores show prominent perspectives for fighting cancers.

The currently reported phototheranostic NIR-II fluorophores can be classified into two categories: inorganic materials and organic materials. Inorganic materials, such as carbon nanotubes,[41–43] quantum dots,[44–46] and rare-earth-doped nanoparticles,[47–49] have poor biocompatibility and reproducibility, slow metabolism, and potential long-term biological toxicity, hindering its further clinical development. Although organic conjugated polymers have good biocompatibility, they also have the problems of difficulty in excretion and uncontrollable molecular weight and structure.[50–55] In contrast, organic small molecule fluorophores have attracted more and more attention due to their controllable molecular structure and performance as well as good biosafety, which have a broader clinical application prospect.[56–60] Herein, we attempt to review the recent progress of organic small molecular NIR-II fluorophores for applications in both cancer diagnosis and treatment. First, the design principles and common central cores of NIR-II small molecular fluorophores will be briefly introduced. Then, we will elaborate each type of NIR-II fluorophores in detail, focusing on the molecular structures and phototheranostic performances, and the future challenges and prospects of them are finally discussed.

DESIGN PRINCIPLES AND COMMON CORES FOR SMALL MOLECULAR NIR-II FLUOROPHORES

The mechanism of fluorescence emission can be roughly divided into three steps. First, the ground state (S_0) fluorophore absorbs certain photo-energy upon irradiation to jump to the excited state (S_n). Second, the excited state decays to the lowest singlet state (S_1) via the processes of internal conversion and vibrational relaxation. Third, the fluorophore at the lowest singlet state S_1 returns to the ground state S_0 by releasing energy in the form of photon radiation. The outgoing light is named fluorescence. Generally, NIR-II fluorophores are defined as a class of molecules whose fluorescence emission wavelengths locating in the NIR-II biological window. To construct an ideal small molecular NIR-II fluorophore for high-performance phototheranostics, several main factors should be taken into consideration, including stability, fluorescence emission wavelength, brightness, photothermal conversion efficiency and ROS generation efficiency.[61–64]

For the NIR-II phototheranostic fluorophores, photo/thermal/chemical-stability is the most basic requirement to be achieved. It is also a guarantee for the smooth expression of various diagnostic and therapeutic properties. It is well known that the longer the wavelength of the light, the deeper the

Table 1. Chemical Structures of Common Types of Organic Small Molecular NIR-II Fluorophores and Some Other NIR-II Organic Small Molecules

BBT- and BSBT-based NIR-II fluorophores

SY1100 — CH1055 — Q4

H1 — H3: X = S / SY1080: X = Se — TPB-AZO

Donor = IR-FTP, IR-FGP, IR-FEP, IR-FTAP, IR-FP8P
Fluorescence QY increases

IR-E1, SYL, Dye 3
CQ-4T, H2a-4T, SY-1030

BBT-based NIR-II AIEgens

BPN-BBTD, TB1, BTPPA, XA1
Fluorescence QY increases

HQL2, HL3, 2TT-oC26B, 2TT-oC6B, 2TT-oC610B
NIR-IIb QY increases

Table 1. *Continued*

Cyanine-based NIR-II fluorophores

A   Cyanine-based fluorophores with NIR-I peak emission

ICG   IR-12N3   IRDye800CW   IR-783   IR-820

B   Cyanine-based fluorophores with NIR-II peak emission

Flav7   5H5   FD-1080   IR-1061

CX-1 →(Red-shift)→ CX-2 →(Red-shift)→ CX-3   QT-RGD

BTC982 →(Red-shift)→ BTC1070

IRBTP-B →(ONOO⁻ activation)→ IRBTP-O   Hydro-1080 →(·OH activation)→ Et-1080

DPP-based NIR-II fluorophores

DPP-BDT   DPP-BT

Table 1. *Continued*

BODIPY-based NIR-II fluorophores

Other NIR-II organic small molecules

Table 1. *Continued*
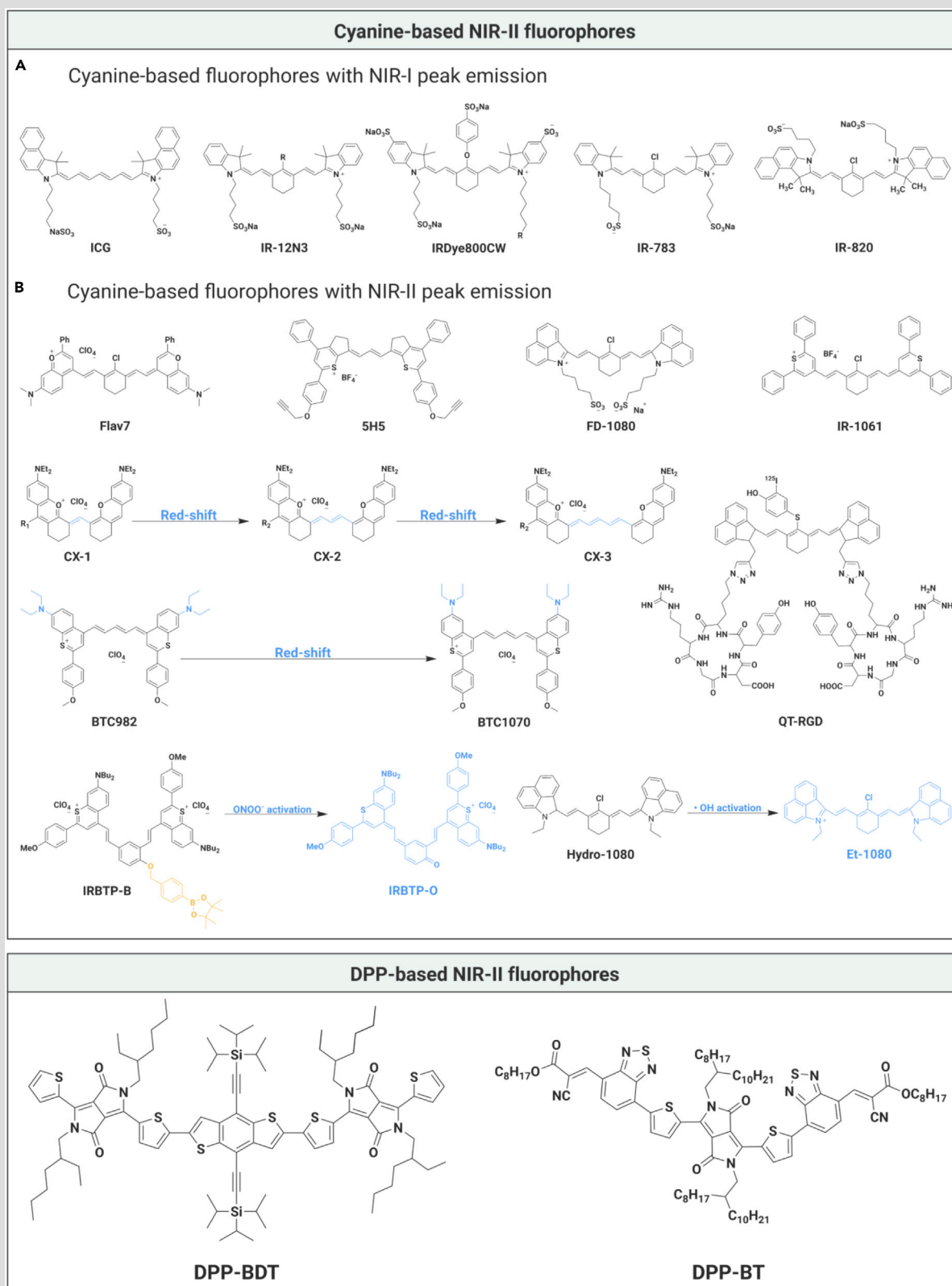
Squaraine-based NIR-II fluorophores

SQP

SQ1
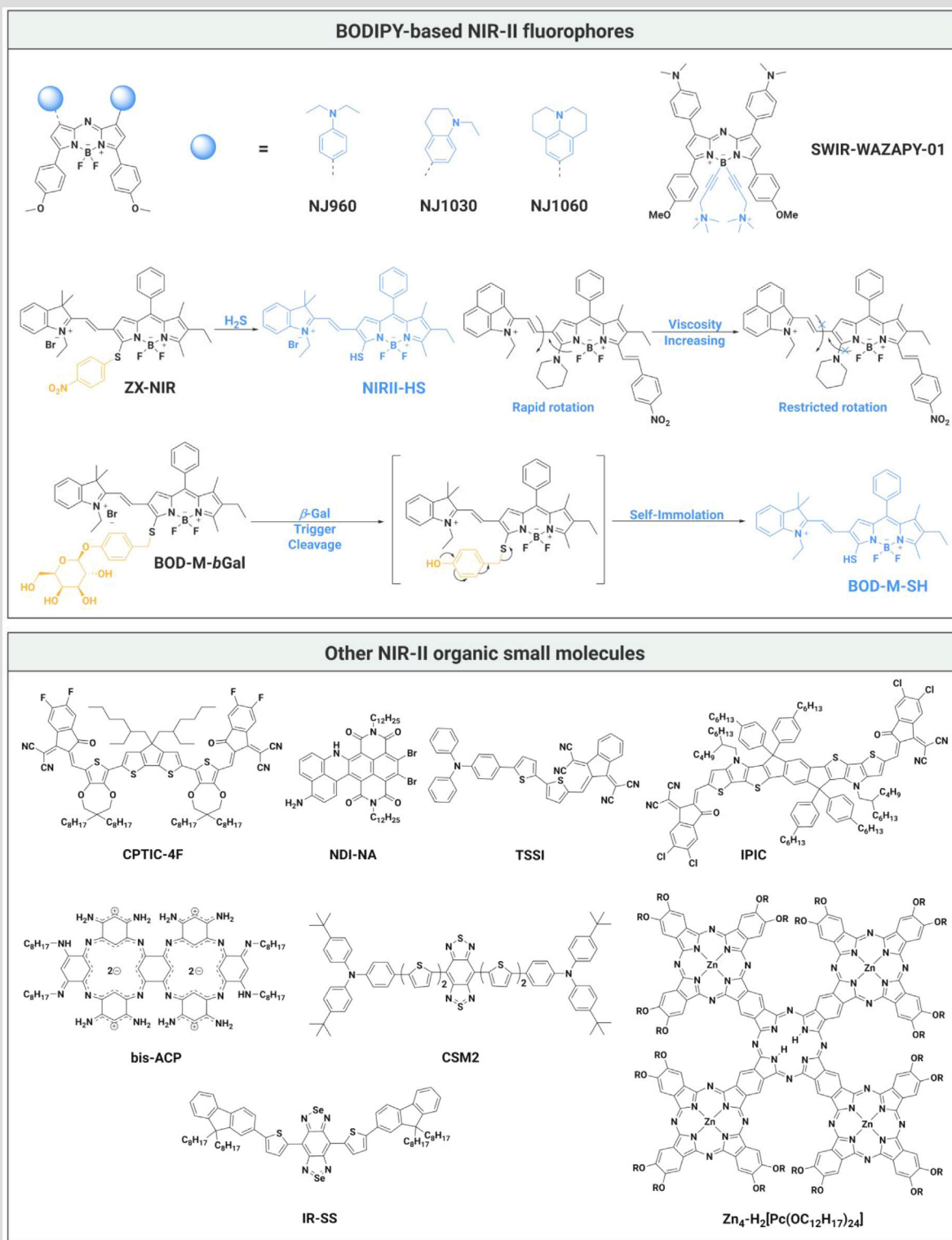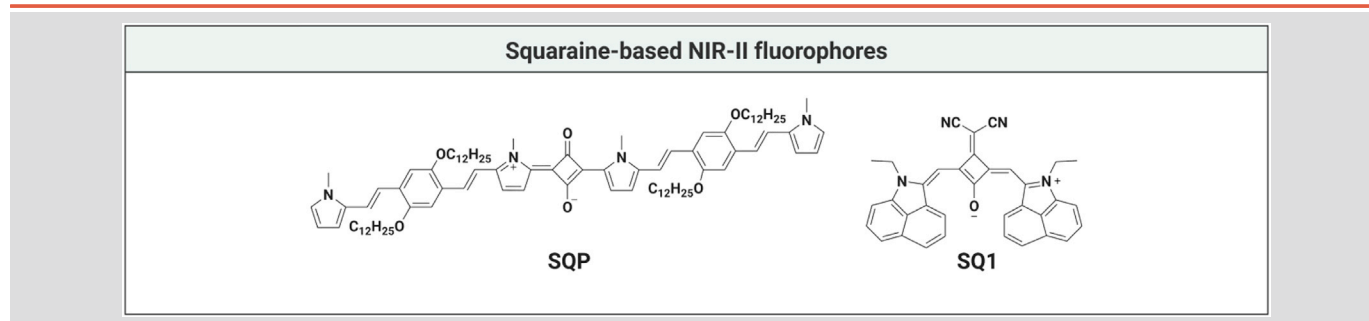
penetration depth, and the lower energy of the photons. Currently, three methods, including the construction of Donor-Acceptor (D-A) motif, the extension of the π-conjugation and quinoidization of the π-system (in some instances), can effectively narrow the highest occupied molecular orbital (HOMO)-lowest unoccupied molecular orbital energy gap (E_g) of the fluorophores. The low E_g will result in a bathochromic shift of their absorbance and fluorescence bands, thereby pushing the fluorescence wavelength to the NIR-II region or even further.[65,66]

Brightness is a parameter of great importance for small molecular NIR-II fluorophores, which will directly affect the imaging performances, such as resolution, imaging speed, etc. Brightness is determined to be the product of fluorescence quantum yield (QY) and absorbance coefficient (ϵ) at the corresponding excitation wavelength. Regarding fluorescence QY, the molecular aggregation of most organic fluorophores at high concentration will quench or weaken the fluorescence emission, which is called the aggregation-caused quenching (ACQ) effect. Therefore, increasing distortion of the molecular structure to decrease the intermolecular interaction is an effective way to improve the fluorescence QY. Furthermore, an opposite concept of the ACQ process, aggregation-induced emission (AIE), has been proposed.[67,68] The fluorophore closely packs to restrict the intramolecular rotations and π-π interactions, switching off the non-radiative transition pathway but switching on the radiative decay pathway. To increase the absorbance coefficient, extension of the π-conjugation with a fused-ring structure is an efficient and practical strategy. However, it can lead to the tendency toward ACQ due to the strong intermolecular π-π interactions. As a result, it is a balance to increase the brightness owing to the paradox between fluorescence QY and absorbance coefficient. Thus, both factors should be optimized simultaneously to achieve high brightness. In addition, to form supramolecular complexes of host-guest or protein-fluorophore is another way to optimize the fluorophore's brightness.[69–72]

It is generally believed that S_1 molecules have three different energy dissipation pathways, accordingly returning to S_0. The fluorescence generation is attributed to the radiative transition of energy from S_1 to S_0. On the contrary, the non-radiative transition is usually accompanied by the generation of heat. Besides, S_1 molecules can also reach the lowest triplet state (T_1) through the intersystem crossing (ISC) process and produce phosphorescence in the form of photon radiation. Meanwhile, the transfer of energy (Type II reaction) can generate $^1O_2$, and other ROS can be produced through electron transfer (Type I reaction). In the process of energy dissipation, such three pathways are always in a competitive relationship.[73] Therefore, blocking a certain pathway can enhance the corresponding performance of other pathways. However, up to now, there is still a lack of effective methods to regulate the photothermal conversion efficiency and ROS generation efficiency of organic small molecular NIR-II fluorophores.

Water dispersibility is another vital issue to be solved for further biological applications *in vivo*. However, most organic small molecular NIR-II fluorophores that have been developed until now are hydrophobic ones. And three common strategies are currently employed to address this issue. One is to directly modify the fluorophores with hydrophilic groups (such as

PEGylated and sulfonated); the modified molecules not only have good water solubility but also usually show the advantages of easy excretion and good biosafety. Another strategy is to fabricate water-soluble nanoparticles (NPs) via self-assembly with the amphiphilic polymeric matrix. These NPs usually present the characteristics of extended blood circulation time, improved tumor uptake, and boosted drug loading capacity, which are not available in the water-soluble groups-modified molecules. The third is to form a nanosized hydrophilic complex with biomacromolecules such as peptides or proteins.[74]

Recently, several types of organic small molecular NIR-II fluorophore have been reported, including Benzobisthiadiazole (BBT), selenadiazolo[3,4-*f*]benzo[*c*][1,2,5] thiadiazole (BSBT), cyanine, Dipyrromethene boron difluoride (BODIPY)/aza-BODIPY, Diketopyrrolopyrrole (DPP), and squaraine-based NIR-II fluorophores. Some other NIR-II organic small molecules have also emerged.

NIR-II ORGANIC SMALL MOLECULAR FLUOROPHORES
BBT-based NIR-II fluorophores

The D-A structured fluorophores have attracted considerable research interest owing to their outstanding photophysical properties. As first reported by Ono et al., in 1994, BBT is a 14 π electron system with a hypervalent sulfur atom and one of the most robust electron-withdrawing building blocks for low bandgap compounds construction.[75] With the rapid development of organic electronics, BBT-based D-A type molecules have been widely synthesized for organic light-emitting diodes, organic photovoltaics, and biophotonics.[76–79] Recently, a series of BBT-based NIR-II fluorophores have been successfully exploited for cancer imaging and phototherapy (Table 1).[80,81]

The first BBT-based NIR-II fluorophore **CH1055** with a molecular weight of 970 Da only was reported in 2016.[82] The electron-rich triphenylamine moiety was used as a donor unit to construct the D-A-D structure. Further PEG-functionalization was performed on the four periphery carboxylic acid groups (-COOH) of **CH1055** to prepare **CH1055**-PEG with improved water solubility and showed rapid renal excretion (~90% metabolized by kidneys within 24 hr) (Figure 1A, Table 2). The brain vasculature imaging with **CH1055**-PEG showed a higher SBR than the clinically approved indocyanine green (ICG) (Figure 1B). Moreover, an anti-epidermal growth factor receptor (EGFR) affibody was conjugated onto **CH1055** to afford **CH1055**-EGFR for active tumor-targeting molecular imaging (Figures 1C and 1D). Fluorophore **CH1055** not only has great potential for precise imaging-guided tumor treatment but also provides a good platform for the further design and construction of BBT-based NIR-II fluorophores, which brings a new era for the study of NIR-II fluorescence.

To expand the library of D-A-D scaffold NIR-II fluorophores and push the fluorescence wavelength more red-shifted, a D-π-A-π-D fluorophore **Q4** was prepared by Sun et al.[83] The thiophene unit was introduced as the π-spacer between triphenylamine (D) and BBT (A) to facilitate intramolecular charge transfer (ICT). However, due to π-π stacking, the fluorescence QY of **Q4** was still unsatisfactory. To surmount this problem, another two fluorophores **H1** and **H3** were prepared by introducing fluorene as
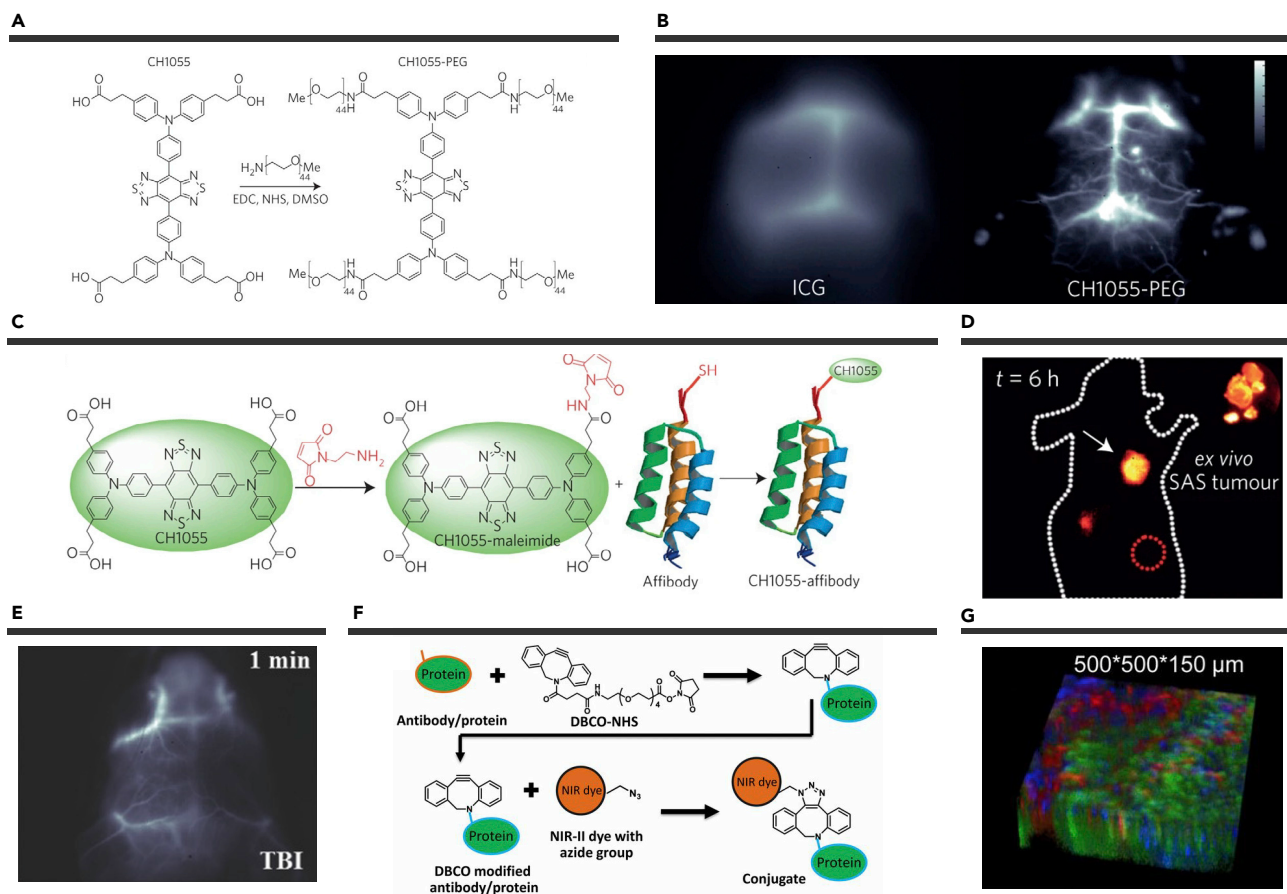
Figure 1. Functional Design and Bioimaging of Small Molecular NIR-II Fluorophores (A) Synthesis of **CH1055**-PEG. (B) Comparison of brain vasculature imaging of ICG in the NIR-I area and **CH1055**-PEG in the NIR-II area. (C) Synthetic schematic diagram of **CH1055**-affibody. (D) Tumor targeted imaging of **CH1055**-EGFR. Reproduced with permission from Li et al.[4] Copyright 2019 Royal Society of Chemistry. (E) Traumatic brain injury imaging of **IR-E1**. Reproduced with permission from Zhang et al.[86] Copyright 2016 Wiley-VCH. (F) Schematic diagram of **IR-FGP** and protein binding through click reaction. Reproduced with permission from Wan et al.[22] Copyright 2019 Wiley-VCH. (G) Three-color 3D rendering of nucleus, neuron, and vessel channels obtained with NIR-I/NIR-II confocal microscopy by using **IR-FGP**. Reproduced with permission from Tu et al.[16] Copyright 2019 Elsevier.

the donor unit, or further replacing thiophene with 3,4-ethoxylene dioxythiophene (EDOT) as the π-bridge.[84,85] With the installation of alkylated fluorene and EDOT, the intermolecular distance was increased to boost the fluorescence QY.

The D-A-D structured NIR-II fluorophores usually possess a large π-conjugated framework to emit fluorescence in the NIR-II biological window. However, such a large π-system will severely cause intermolecular interactions and aggregation. The interaction between water molecules and organic fluorophores is the main reason for the quenching of the fluorophores' excited states, resulting in a low fluorescence QY in aqueous solutions. To overcome these problems, researchers have put forward the shielding units (S) to flank at the periphery sites to construct the S-D-A-D-S scaffolds. The shielding units can effectively reduce the intermolecular interactions and then protect the excited state molecules from the interference of water molecules.

The first S-D-A-D-S structured NIR-II fluorophore **IR-E1** was reported in 2016.[86] The BBT acceptor and thiophene/EDOT donor were used to construct the D-A-D structure to endow the fluorophore a low E_g. Meanwhile, EDOT as the π-bridge between the thiophene and BBT can result in molecular distortion and decrease the intermolecular aggregation. The 2,6-alkoxyl-substituted benzene was also applied as the shielding unit to prevent the interaction with water molecules. Furthermore, **IR-E1** showed a higher fluorescence QY of 0.07% than **CH1055** (0.03%) and was applied for NIR-II fluorescence imaging of cerebrovascular injury in a mouse model with traumatic brain injury (Figure 1E).

Based on **IR-E1**, NIR-II fluorophore **IR-BGP6** was developed by replacing the donor unit with tert(ethylene glycol) (TEG)-substituted thiophene. Due

to the introduction of TEG-substituted thiophene, **IR-BGP6** obtained good water solubility and rapid renal excretion capacity ($\sim$91% excretion within 10 h). The inherent S-D-A-D-S structure made it exhibit a relatively high fluorescence QY ($\sim$0.15%). **IR-BGP6** was further conjugated with the programmed cell death ligand-1 monoclonal antibody (PD-L1 mAb) for targeted imaging of MC38-overexpressed immune checkpoint PD-L1. This work provides a practical way to construct NIR-II fluorophore with rapid renal excretion ability for molecular imaging *in vivo*.[87]

In another work, TEG-substituted thiophene was introduced as a donor unit again. In addition to distorting the π-conjugated backbone, TEG-thiophene could also increase the dihedral angle between donor and acceptor in comparison to triphenylamine, EDOT, and thiophene units. The dialkyl chain-substituted fluorene could act as the protecting group to avoid intermolecular interactions. Fluorophore IR-FGP showed an enhanced fluorescence QY of 0.19% in an aqueous solution.[88] When coupled with a dibenzocyclooctyne (DBCO)-PEG4-NHS ester connector, the -N$_3$ group on the fluorophore could conjugate a protein or an antibody for 3D-staining of $\sim$170 μm histological brain tissues sections (Figures 1F and 1G).

Although these efforts have achieved significant progress, there still has much space to improve the fluorescence QY in aqueous solutions. Inspired by **IR-E1** and **IR-FGP**, EDOT and dialkyl fluorene were introduced into the **BBTD** backbone to develop the NIR-II fluorophores **IR-FE/IR-FEP**.[89] Another two families of fluorophores **IR-FT/FTP** and **IR-BBE/BBEP** were prepared as well. **IR-FE** and **IR-FEP** presented the fluorescence QY of 3.1% in toluene and 0.2% in the aqueous solution, respectively. Compared with **IR-FTP**, the fluorescence QY of **IR-FEP** in

Table 2. BBT- and BSBT-based NIR-II Fluorophores

Fluorophore	Hydrophilic Modification	Targeted Modification	$\lambda_{Abs}/\lambda_{em}$ (nm)	QY[a]	Imaging Strategy	Therapeutic Mode	Biological Applications	Ref
CH1055	PEGylated	EGFR affibody conjugate	750/1,055	0.03% in water	FLI	/	Vessel, lymph node, and tumor imaging	Antaris et al.[82]
Q4	DSPE-mPEG$_{5k}$	GRPR peptide conjugate	N.A./1,100	0.02% in water	FLI	/	Vessel imaging; prostate cancer imaging	Sun et al.[83]
H1	DSPE-mPEG$_{5k}$ or PEGylated	mono-c(RGDfk) peptide conjugate	N.A./1,100	0.20% in DCM	FLI	/	Vessel and whole-body imaging	Sun et al.[84]
H3	PEGylated	/	760/1,023	1.23% in DCM	FLI	/	DMBA-induced carcinoma imaging and imaging-guided surgery	Zeng et al.[85]
IR-E1	PEGylated	/	N.A./1,071	0.07% in water	FLI	/	Traumatic brain injury imaging	Zhang et al.[86]
IR-BGP6	PEGylated	PD-L1 affibody conjugate	736/1,047	0.15% in water	FLI	/	Tumor-targeting imaging	Wan et al.[87]
IR-FGP	PEGylated	EGFR affibody conjugate	745/1,050	0.19% in water	FLI	/	Brain tissue neuron imaging	Zhu et al.[88]
IR-FEP	PEGylated	/	780/1,047	0.20% in water	FLI	/	Vessel and tumor imaging	Yang et al.[89]
IR-FTAP	PEGylated	/	733/1,048	0.53% in water	FLI	/	Hindlimb vessel imaging	Yang et al.[90]
IR-FP8P	PEGylated	FSH conjugate	748/1,040	0.60% in water	FLI	/	Ovary imaging	Ma et al.[91]
CH-4T	Sulfonated; FBS	/	738/1,055	0.50%−1.10% in serum	FLI	/	Vessel and lymph node imaging	Antaris et al.[92]
H2Ha-4T	Sulfonated; FBS	Cetuximab complex	738/1,024	0.01% in water; up to 0.11% in serum when heated	FLI/PTI	PTT	Hindlimb vessel and the lymphatic imaging; imaging-guided sentinel lymph node surgery and colorectal cancer PTT	Zeng et al.[93]
Q8PNap	PEGylated; FBS	/	N.A.	0.003% in water; up to 0.0114% in serum when heated	FLI	/	Hindlimb vessel, lymphatic system, and tumor metastasis imaging; imaging-guided tumor and lymph node surgery	Qu et al.[94]
CQ-4T	Sulfonated; HSA	/	N.A.	0.104% in PBS; 0.34% in HSA	FLI	/	Monitoring thrombosis, peripheral arterial disease, tumor angiogenesis, and lymphatic drainage; imaging-guided tumor resection and sentinel lymph node biopsy	Li et al.[95]
p-FE	PS-g-PEG	/	760/1,010	1.65% in water	FLI	/	3D vessel imaging and tumor imaging	Wan et al.[96]
TPB-AZO	PS-PEG	/	690/909	1.562% (850−1,500 nm); 0.351% (1,000−1,500 nm)	FLI	/	Determining cardiac cycle and heart rate; tumor detection	Zhang et al.[97]
SYL	DSPE-mPEG$_{5k}$	/	765/976	N.A.	FLI/PAI	PTT	Tumor imaging and imaging-guided PTT	Zhang et al.[99]
BPN-BBTD	F127	/	700/949	0.18% (>1,000 nm)	FLI	PTT	Tumor imaging and imaging-guided PTT, long-term tumor monitoring	Alifu et al.[102]
TB1	DSPE-mPEG$_{2k}$	Decorated with c-RGD	740/975	0.62%	FLI/PAI	/	Brain tumor imaging	Sheng et al.[103]
BTPPA	DSPE-mPEG$_{2k}$	/	761/1,013	0.99%; 0.60% (>1,000 nm)	FLI	/	Hindlimb, cerebral, lymph vessel, and tumor imaging	Wu et al.[104]
XA1	F127	/	780/1,000	1.48%	FLI	/	Hindlimb, cerebral, and tumor imaging	Xu et al.[105]

(Continued on next page)

Table 2. *Continued*

Fluorophore	Hydrophilic Modification	Targeted Modification	$\lambda_{Abs}/\lambda_{em}$ (nm)	QU[a]	Imaging Strategy	Therapeutic Mode	Biological Applications	Ref
HOL2	DSPE-mPEG$_{5K}$	/	710/1,050	1.19% (>1,000 nm); 0.016% beyond 1,300 nm; 0.002% beyond 1,550 nm	FLI	/	Vessel and tumor imaging	Li et al.[107]
HL3	DPPE-5KPEG	/	750/1,050	1.17% (>1,000 nm); 0.005% in the NIR-IIb	FLI	/	Whole-body, cerebral vessel, and lymph node imaging	Li et al.[108]
2TT-Oc26b	DSPE-mPEG$_{2k}$	/	700/1,030	1.15% (>1,000 nm); 0.012% in the NIR-IIb	FLI	/	Whole-body, cerebral vessel, and intestinal trace imaging	Li et al.[109]
SY1080	DSPE-PEG$_{5K}$	/	820/1,080	0.15% in THF	FLI/PAI	PTT	Tumor imaging and imaging-guided PTT	Zhang et al.[110]

[a]Fluorescence quantum yields of all small molecular NIR-II fluorophores mentioned in this review were recalculated based on IR26 = 0.05% (in 1,2-dichloroethane).

aqueous solution was significantly improved by 100-fold. This work has confirmed that both EDOT and the shielding unit of fluorene can improve fluorescence QY in aqueous solution, and EDOT is superior to thiophene for the fluorescence QY enhancement.

Based on **IR-FTP**, S-D2-D1-A-D1-D2-S structured fluorophore **IR-FTAP** was prepared by introducing octylthiophene donor as the first donor between the second donor thiophene and **BBTD** acceptor.[90] Thiophene as the second donor could extend the conjugation length, which would cause red-shift but lower fluorescence QY. Compared with the π-bridge units previously studied, such as thiophene, TEG-thiophene, and EDOT, the bulky and hydrophobic octylthiophene group could cause a larger conjugated backbone distortion. Thus, **IR-FTAP** exhibited an emission peak at 1048 nm and fluorescence QY of 0.53% in aqueous solution. The fluorescence QY of **IR-FTAP** was higher than all their previously reported water-soluble S-D-A-D-S structured NIR-II fluorophores. Using **IR-FTAP**, the fast (>25 frames/s) NIR-II imaging with high resolution was realized.

To construct S-D-A-D-S structure is an effective strategy to improve fluorescence QY in aqueous solution. However, the absorption coefficient of these fluorophores is not very high, which restricts their brightness for NIR-II fluorescence imaging. To address this issue, Ma et al. reported another NIR-II fluorophore **IR-FP8P** by introducing a novel donor unit, dioctyl chains substituted 3,4-propylenedioxy thiophene (PDOT).[91] Compared with the octylthiophene of **IR-FTAP**, PDOT donor had less capability to distort the conjugated backbone. Thus, **IR-FP8P** exhibited a red-shifted absorption peak and a larger absorption coefficient. Meanwhile, the dioctyl chains could protect the backbone from the attack of water molecules to improve the fluorescence QY. **IR-FP8P** with an emission peak at 1,040 nm presented a fluorescence QY of 0.6% and a peak absorption coefficient of 1.3×10^4 $M^{-1} \cdot cm^{-1}$ in aqueous solution. Compared with **IR-FEP** and **IR-FTAP**, the brightness of **IR-FP8P** increased 5.7-fold and 3.7-fold, respectively. Owing to the high brightness, **IR-FP8P** could be applied for video-rate NIR-II imaging at 1,300 nm long-pass filter.

The coating strategy of fluorophore-protein complex formation can also improve the brightness of NIR-II fluorophores. In 2017, Antaris et al. replaced the flanked carboxyl groups of **CH1055** with sulfonate to develop a new NIR-II fluorophore **CH-4T** (Figure 2A).[92] Due to the negatively charged sulfonate groups, **CH-4T** could bind to serum proteins via supramolecular self-assembly. The fluorescence intensity of supramolecular assemblies (QY of ∼0.5%) was dramatically increased by ∼50-fold compared with that of **CH-4T** in PBS (Figure 2B). Simply heating to 70°C for 10 min, the fluorescence QY of the **CH-4T**-protein complexes could be boosted from 0.5% to 1.1% (Figure 2C). This may be attributed to the fact that heating could promote the exposure of **CH-4T** to hydrophobic regions inside the serum protein. Under heating conditions, the brightness of **CH-4T**/fetal bovine serum (FBS) was significantly improved by 110-fold compared with **CH-4T**/PBS. **CH-4T**/FBS enabled the ultrafast NIR-II fluorescence imaging with 50 frames/s and ∼1.5−2 ms exposure times, which was used to resolve cardiac cycles of mice.

Inspired by this work, another sulfonated NIR-II fluorophore **H2a-4T** was reported by Zeng et al.[93] Compared with **H2a-4T** in water, the fluorescence intensity of **H2a-4T**@FBS was significantly enhanced by approximately 10-fold at room temperature. The fluorescence QY of **H2a-4T**@FBS could be boosted to ∼0.11% after heating to 70°C for 10 min. Further, the **H2a-4T**@Cetuximab complex was developed for antibody-targeted imaging-guided PTT of colon cancer (Figure 2D). In another work, the fluorophore **Q8** was modified with PEG$_{2000}$ to improve water solubility.[94] However, the pronounced twisted intramolecular charge transfer (TICT) effect weakened the fluorescence signals. To mitigate the TICT effect, the *N,N*-dialkylamino unit of **Q8P** was converted to quaternary ammonium salts (Figure 2E). After mixed with FBS, the fluorescence QY was dramatically enhanced ∼32-fold. Li et al. also reported a sulfonated NIR-II fluorophore **CQ-4T** and mixed it with human serum albumin (HSA).[95] Compared with **CQ-4T** alone, the complexes of **CQ-4T**/HSA showed better optical performances and a 6.65-fold enhancement in fluorescence intensity. Because of the excellent brightness and optical properties of **CQ-4T**/HSA, the *in vivo* real-time imaging of circulatory system-related disease processes and precise surgery under imaging navigation was achieved (Figure 2F).

Besides to the serum proteins, Wan et al. also innovatively designed a novel amphiphilic polymer matrix (PS-*g*-PEG) to increase fluorescence QY in aqueous solutions (Figure 3A).[96] The previously reported **IR-FE** showed a high fluorescence QY of 3.1% in toluene. The hydrophobic interior of PS-*g*-PEG with a phenyl group could imitate an environment similar to the toluene solvents. Meanwhile, the hydrophilic PEG chains on the polymer matrix could provide good water solubility and biocompatibility. After encapsulating **IR-FE** with PS-*g*-PEG, the fluorophore (**p-FE**) presented an unprecedented high fluorescence QY of ∼1.65% in aqueous solution. This high brightness fluorophore was applied to single-photon-based 3D confocal imaging with an imaging depth up to ∼1.3 mm and a high spatial resolution of sub-10 μm (Figure 3B). Moreover, the fast NIR-II imaging of blood flow in brain vessels was achieved with 2 ms exposure time. This work offers an extremely effective strategy to retain high fluorescence QY in aqueous solutions.

Similar to this, another NIR-II fluorophore **TPB-AZO** also showed a high fluorescence QY of ∼2.159% in toluene.[97] Encapsulated by PS-*g*-PEG, **TPB-AZO** presented fluorescence QY of ∼1.562% within 850 to 1,500 nm and ∼0.351% within 1,000−1,500 nm in aqueous solution. As demonstrating the effectiveness of PS-*g*-PEG encapsulation to impart a non-polar toluene-like circumstance to impede ACQ for fluorescence QY enhancement. TPB-AZO NPs was used for fast imaging (>26 frames/s) of heart rate and cardiac cycle of mice.

Another amphiphilic DNA block copolymer (PS-*b*-DNA) was reported by Xiao et al. (Figure 3C).[98] Through self-assembly, PS-*b*-DNA could form the micelle structure with many typical features of spherical nucleic acid (SNA). The PS-*b*-DNA SNA was capable of the blood-brain barrier (BBB)-crossing via cell membrane-bound scavenger receptor-mediated
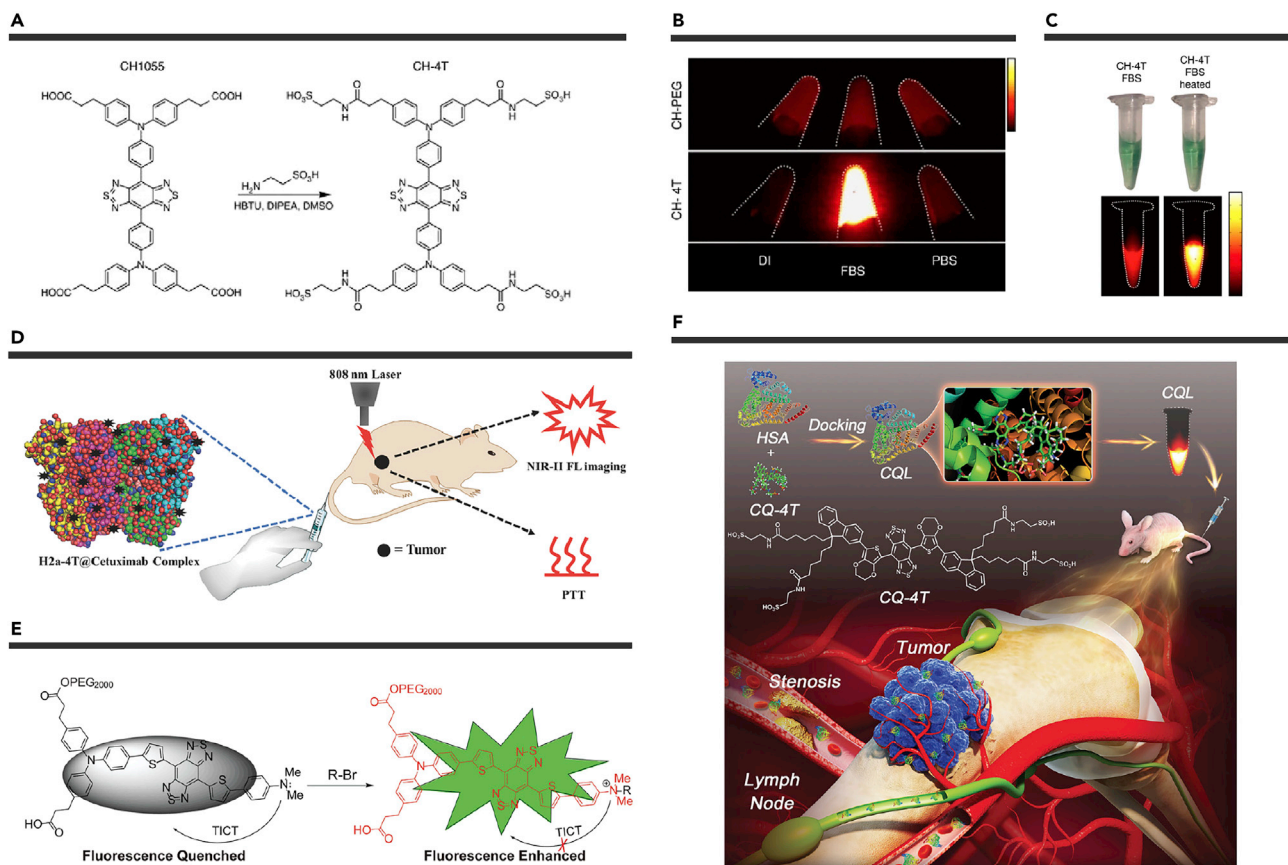
Figure 2. Construction and Biological Applications of Fluorophore-Protein Complexes (A) Synthesis of **CH-4T**. (B) NIR-II fluorescence images of CH-PEG and **CH-4T** in deioni1zed water, FBS, and PBS. (C) Photographs and corresponding NIR-II fluorescence images of **CH-4T** in FBS and heated FBS. Reproduced with permission from Antaris et al.[92] Copyright 2017 Springer Nature. (D) Schematic of **H2a-4T**@Cetuximab complex used in NIR-II fluorescence imaging and PTT. Reproduced with permission from Zeng et al.[93] Copyright 2018 Wiley-VCH. (E) The schematic explanation for fluorescence enhancement by introducing quaternary ammonium salts. Reproduced with permission from Qu et al.[94] Copyright 2019 Wiley-VCH. (F) Schematic of **CQ-4T**/HSA complex for multifunctional biomedical imaging and surgical navigation in the NIR-II area. Reproduced with permission from Li et al.[95] Copyright 2019 Wiley-VCH.

endocytosis. To further increase the accumulation in brain tumor sites, a targeting aptamer was taken to hybridize with DNA in PS-*b*-DNA. Finally, the nanofluorophore was prepared via loading **IR-FE** into the hydrophobic core. Compared with **IR-FE** encapsulated by the normal PS-*b*-PEG, the fluorescence intensity of this aptamer-modified PS-*b*-DNA nanofluorophore at the brain glioblastoma site showed a 3.8-fold enhancement (Figure 3D). This innovative work provides an excellent strategy to overcome the obstacles of BBB, opening new insights for the diagnosis and treatment of brain tumors.

Given the advantages of NIR-II fluorescence imaging in disease diagnosis, Zhang et al. developed a multifunctional DD-A-DD structured fluorophore **SYL**.[99] **SYL** NPs with an average size of ~120 nm showed an absorption and emission peak at ~765 nm and ~976 nm, respectively. Under the 808 nm laser irradiation, **SYL** NPs presented a photothermal conversion efficiency of ~21.8% and were used for dual-modal NIR-II fluorescence/photoacoustic imaging-guided PTT for tumors.

At present, several practical strategies have been developed to reduce the aggregations of the fluorophore molecules. Nonetheless, most NIR-II fluorophores still suffer from the severe aggregation-induced quenching (ACQ) effect. Opposite to the ACQ effect, an AIE concept was put forward by Tang et al., in 2001.[100] By reducing non-radiative transitions via physically restricting intramolecular rotation, aggregation-induced emissive luminogens (AIEgens) usually present enhanced fluorescence upon aggregates.[101] Based on this, some high brightness NIR-II AIE dots have been designed and prepared (Table 1). For example, Tang et al. reported an AIEgen **BPN-BBTD** by taking *N*, *N*-diphenylnaphthalen-1-amine (BPN) as the donor unit.[102] Under the 785 nm laser irradiation, the ultra-stable **BPN-BBTD** dots showed fluores-

cence QY of ~0.18% in the NIR-II region and photothermal conversion efficiency of 39.8%. Moreover, **BPN-BBTD** dots could monitor the tumor progression for a long duration of 32 days, paving the way for the future application of real-time monitor of tumor treatment and metastasis.

Besides, *N*, *N*-diphenyl-4-(1,2,2-triphenylvinyl)aniline (DPTPEA) was proposed by Sheng et al. as the Donor unit to design an AIEgen **TB1**.[103] The **TB1** dots presented a large absorptivity of 10.2 L g^{-1}·cm^{-1} at 740 nm, and showed an emission peak at 975 nm with fluorescence QY of 0.62%. Then, c-RGD peptide was further decorated to prepare the tumor-specific **TB1**-RGD dots. It is applied for targeted NIR-I PAI and NIR-II fluorescence imaging of brain tumors with an SBR of 4.4 and resolution up to 38 μm, indicating an excellent spatiotemporal resolution. Based on **TB1**, another fluorophore **BTPPA** was prepared via side-chain engineering.[104] The introduction of an octyloxy side-chain impeded the strong intermolecular interaction, not only improving the solubility of **BTPPA** in organic solvents but also enhancing the fluorescence QY of **BTPPA** in aggregated status. Comparing to **TB1** dots, **BTPPA** dots showed a higher fluorescence QY of 0.99% in water. Xu et al. reported a novel D-π-A-π-D type AIEgen **XA1** with triphenylamine as Donor and tetraphenylethene as the molecular rotor.[105] With more twisted molecular conformations to prevent intermolecular π-π interaction, the fluorescence QY of **XA1** dots was determined to be 1.48% in aqueous solution, which was the highest among all the NIR-II AIE dots at present.

In the wavelength range of 1,400 to 1,500 nm, water and tissues have strong absorption of NIR light.[106] To avoid this, the NIR-II imaging window is further divided into three sub-regions: NIR-IIa' (1,000–1,300 nm), NIR-IIa (1,300–1,400 nm), and NIR-IIb
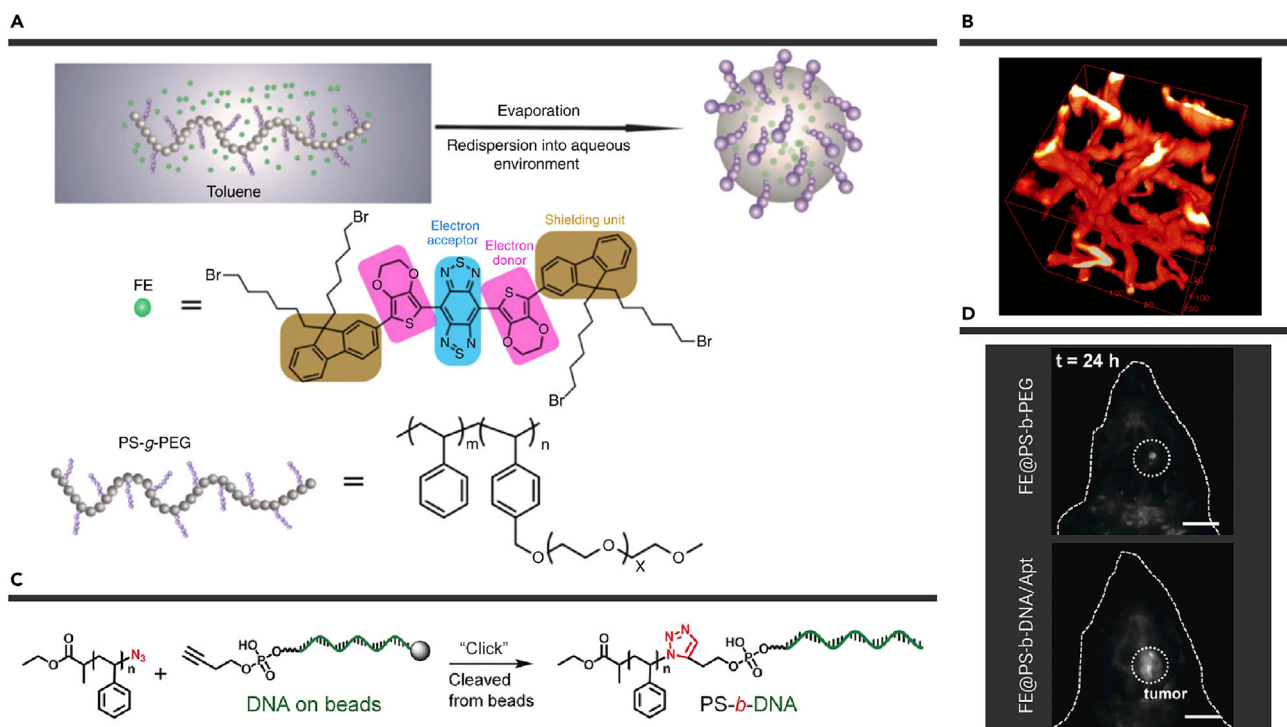
Figure 3. Construction and Biological Applications of FE-based Nanoparticles (A) Chemical structures of **FE** and PS-*g*-PEG and the formation of **p-FE**. (B) 3D reconstruction of vasculatures in brain by using **p-FE**. Reproduced with permission from Wan et al.[96] Copyright 2018 Springer Nature. (C) Synthesis of PS-*b*-DNA polymer. (D) Comparison of mouse brain glioblastoma imaging by using **FE**@PS-*b*-PEG and **FE**@PS-*b*-DNA/Apt. Scale bars: 0.5 cm. Reproduced with permission from Xiao et al.[98] Copyright 2020 Wiley-VCH.

(1,500–1,700 nm). Recently, several NIR-II AIEgens with both long emission wavelength and high fluorescence QY have been exploited to further suppress photo-scattering and autofluorescence for deeper tissue penetration depth and higher resolution (Table 1).

Based on **Q4**, Li et al. developed a highly twisted AIEgen **HQL2** (twist angle of 50.9°) by modifying the dodecyl hydrocarbon chain at different positions of the thiophene spacer.[107] **HOL2** with higher brightness showed an emission peak at ~1,050 nm with the emission profile extended to 1,600 nm. The fluorescence QY of **HOL2** dots in aqueous solution was determined to be 1.19% in the NIR-II regime, and 0.016% beyond 1,300 nm, 0.002% beyond 1,550 nm. The SBR of fluorescence imaging in the NIR-IIa region was 2.5-fold higher than that in the NIR-IIb region, which was mainly owing to the low fluorescence QY in the NIR-IIb region. To optimize the quality of NIR-IIb fluorescence imaging, another highly twisted NIR-II fluorophore **HL3** was prepared with the dihedral angle of 45.5° between acceptor BBT and donor 3,4-bis(hexyloxy)thiophene.[108] The **HL3** dots showed a high fluorescence QY of 1.17% in the NIR-II region and 0.005% in the NIR-IIb region in aqueous solutions. Comparing to **HOL2** dots, the resolution of NIR-IIb fluorescence imaging based on **HL3** dots was improved due to the higher fluorescence QY in the NIR-IIb region (Figure 4A).

Li et al. also elaborated on the design principles of these NIR-IIb AIEgens at the molecular and morphological levels (Figure 4B). Combined with the TICT and AIE effects, another three twisted AIEgens with different flexible hydrocarbon chains on the thiophene unit were developed.[109] Among them, **2TT-oC26B** dots presented a fluorescence tail extending to 1,600 nm with a fluorescence QY up to 1.15% in the entire NIR-II region and fluorescence QY of 0.012% in the NIR-IIb region. By employing **2TT-oC26B** NPs, the NIR-IIb fluorescence imaging displayed a higher imaging resolution and improved SBR. The innovative work provides an extremely effective way for the development of small organic molecules with high brightness and ultra-long emission wavelength.

BSBT-based NIR-II Fluorophores

The selenium-substituted analog of BBT building block, selenadiazolo[3,4-*f*]benzo[*c*][1,2,5] thiadiazole (BSBT), is another strong electron-acceptor, which can also be used to construct NIR-II fluorophores through the D-A-D strategy. The heavier selenium (Se) atoms substitute one sulfur atom of BBT acceptor can realize a pronounced red-shift in absorption and emission bands (Table 1).

Zhang et al. reported a multifunctional BSBT-based fluorophore **SY1080**.[110] To solve the blue-shift problem caused by the introduction of the EDOT unit, a selenium atom was introduced to regulate the brightness and emission wavelength. **SY1080** showed an emission peak at 1,080 nm, and the NIR-II fluorescence signal was higher than **H1** in THF. The fluorescence QY of **SY1080** was determined to be 0.15% in THF. Around 820 nm, **SY1080** presented a strong fluorescence absorption peak, which suggested it could convert a part of optical energy into heat for cancer therapy. To obtain water solubility and biocompatibility, **SY1080** NPs were prepared with a photothermal conversion efficiency of ~22.3%, and applied for NIR-II fluorescence/photoacoustic imaging-guided PTT of the tumor.

Traditional drug chemotherapy is nonspecific and has toxic side effects on normal tissues and cells. To solve this problem, they also designed another integrated diagnostic and therapeutic nano-agent by encapsulating the Pt(II) metallacycle and BSBT-based NIR-II fluorophore **SY1100** into DSPE-*m*PEG$_{5k}$ (Figure 4C).[111] Under the tracking of NIR-II FLI, the nano-agent could selectively deliver the Pt(II) metallacycle to the tumor sites via the enhanced permeability and retention (EPR) effect and presented a better anti-tumor activity than cisplatin alone. This strategy of simultaneously loading chemotherapy drugs and imaging molecules into the carrier can not only achieve effective treatment to reduce side effects, but also monitor the size of the tumor in real-time.

Cyanine-based NIR-II Fluorophores

Cyanine fluorophores start with the traditional NIR-I fluorophore ICG, which has been approved by the U.S. Food and Drug Administration (FDA) for
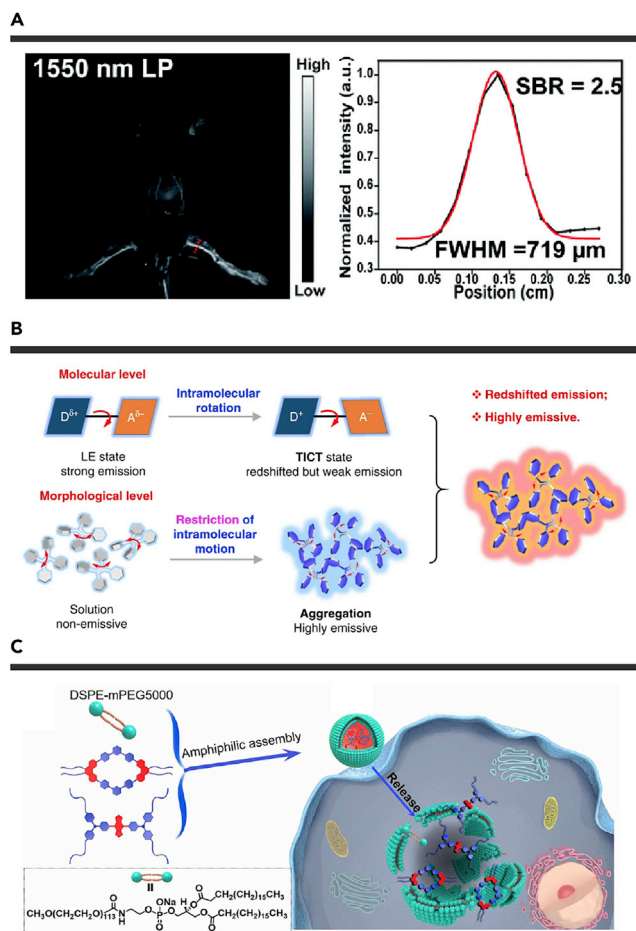
Figure 4. Applications of Small Molecular NIR-II Fluorophores in NIR-IIb Imaging and Drug Delivery Monitoring (A) NIR-IIb fluorescence images of whole mouse blood vessels at 1,550 nm long-pass filters using **HL3** dots. Reproduced with permission from Li et al.[108] Copyright 2020 Royal Society of Chemistry. (B) The design strategy of small molecular NIR-IIb fluorophores. Reproduced with permission from Li et al.[109] Copyright 2020 Springer Nature. (C) Schematic of the cellular uptake of self-assembled nanoprobe. Reproduced with permission from Sun et al.[111] Copyright 2019 National Academy of Sciences.

clinical applications in humans. With a tail emission extending to the NIR-II region, ICG has been applied to NIR-II fluorescence imaging.[112,113] Besides ICG, some other cyanine fluorophores with the primary emission in the NIR-I window, such as **IR-12N3**, **IRDye800CW**, **IR-783**, and **IR-820**, also have the potential for NIR-II fluorescence imaging (Table 1).[114–116] Although these fluorophores could be employed for NIR-II fluorescence imaging, the NIR-II emission is not very ideal, which limits the further improvement of NIR-II fluorescence imaging quality. Thus, certain cyanine-based NIR-II fluorophores have been exploited by extending π-conjugation or embedding heterocycle substitutions (Table 1).[117]

The NIR-II polymethine fluorophore **Flav7** was first reported in 2017 by introducing the 7-dimethylamino flavylium heterocycle (Table 3).[118] **Flav7** showed the absorption and emission peaks at 1,026 nm and 1,045 nm, respectively. Under the 808 nm laser irradiation, **Flav7** presented a 13-fold higher brightness than that of IR-26 in DCM. This pioneering work opens the door for the development of cyanine-based NIR-II fluorophores. Inspired by the structure of ICG, a polymethine thiopyrylium fluorophore **5H5** was reported by Hong's group in 2018.[119] By introducing sulfur atoms into the polymethine backbone, **5H5** showed an absorption peak at 1,069 nm, an emission peak at ~1,125 nm and a shoulder emission peak at ~1,260 nm. Moreover, the tail emission of **5H5** extended to 1,400 nm. By using **5H5**, NIR-IIa fluorescence imaging under 1,064 nm laser irradiation was readily achieved.

In 2018, cyanine fluorophore **FD-1080** with heptamethine structure was prepared and presented both NIR-II absorption and fluorescence.[120] To improve the water solubility and stability of this fluorophore, the sulfonic and cyclohexene groups were further introduced. **FD-1080**, with a small molecular mass of 760 Da, was capable of fast kidney metabolism and presented an absorption and emission peak at 1,064 nm and 1,080 nm, respectively. The fluorescence QY of **FD-1080** was 0.31% in ethanol. After encapsulation by FBS to form a complex, the fluorescence QY could increase to 5.94%. Compared with the common NIR excitation, the imaging under NIR-II excitation presented a deeper tissue penetration and higher resolution. **FD-1080** could not only perform high-performance hindlimb and brain vessel imaging, but also quantify the respiration frequency of mice by dynamic imaging (7.16 frames/s). Furthermore, the J-aggregates were prepared through self-assembly between 1,2-dimyristoyl-sn-glycero-3-phosphocholine (DMPC) lipids and **FD-1080**.[121] The **FD-1080** J-aggregates presented an absorption and emission peak at 1,360 nm and 1,370 nm, respectively. Using the J-aggregates, the NIR-IIb dynamic imaging of hindlimb vessels and brain was achieved and showed a superior SBR and high resolution.

Besides **FD-1080** and its J-aggregates, a panel of novel polymethine dyes **CX-1**, **CX-2**, and **CX-3** were prepared by extending the π-conjugation length of the backbone.[122] With the increase of the π-conjugated C=C units, pronounced red-shift of both absorption and fluorescence was observed. By using **CX-1** and **CX-3**, peroxynitrite (OONO⁻) could be detected via Förster resonance energy transfer (FRET) process in the acetaminophen (APAP)-induced liver injury model.

To address the problem of solvatochromism-caused quenching in water, Wang et al. also developed another two photo-stable pentamethine cyanine fluorophores, **BTC982** and **BTC1070**, with the anti-quenching behavior.[123] By changing the position of the diethylamino (-NEt₂) groups on the phenyl ring from the meta-position to the para-position, a pronounced red-shift could be realized. In comparison to IR26 in aqueous solution, **BTC1070** and **BTC982** showed ~7-fold and ~44-fold enhanced brightness, respectively. As the pH changed from 1 to 4, the ratiometric fluorescence of **BTC1070** could change from 1,065 nm to 980 nm. By taking **BTC1070**, the gastric pH assessment at 4 mm depth was realized, and reliable accuracy was comparable to that of the standard pH meter.

At present, most NIR-II fluorophores, whether with passive tumor-targeting or active tumor-targeting behavior, belong to the "always-on" type. This type of "always-on" fluorophores produces fluorescent signals all the time, whether it is in the lesion or accumulated in normal tissues. The "always-on" fluorescent signal will cause a low target-to-background ratio or even false positive, which is a severe problem for biosensing, disease diagnosis, and cancer treatment.[124] In this perspective, "turn-on" type fluorophores are in urgent need for both academy and industry. Li et al. developed an ONOO⁻ activatable NIR-II fluorophore **IRBTP-B** via combining the benzothiopyrylium cyanines backbone with the phenyl borate.[125] Under the activation of ONOO⁻, the NIR-II fluorescence could be lighted up when **IRBTP-B** converted into another fluorophore **IRBTP-O** by eliminating the phenyl borate unit (Table 1). Further research showed the high selectivity toward ONOO⁻, since some other in vivo factors, such as biothiols, ROS, and reactive nitrogen species had almost no effect on this transformation process. In addition, the activated fluorescence signal could be detected at a depth of 5 mm. By using this fluorophore, ONOO⁻ could be effectively and selectively detected to monitor the preclinical APAP-induced liver injury.

Feng et al. reported an ·OH-activatable NIR-II fluorescent probe **Hydro-1080**.[126] Due to the low π-conjugation and non-planarity, **Hydro-1080** showed a weak absorption in the visible region and even no fluorescence emission (Table 1). In the presence of ·OH, both π-conjugation and planarity of **Hydro-1080** were significantly improved. The activated molecule **Et-1080** showed an absorption and emission peak at 1039 nm and 1080 nm in DMSO. The ·OH-activatable probe could accurately and selectively identify the ·OH species. Moreover, the subtle changes of ·OH content in the liver injury model could be tracked under NIR-II fluorescence imaging.

Besides the single pathological parameter activatable probes, Tang et al. reported a dual pathological parameter activatable nanoprobe (Figure 5A).[127]

Table 3. Cyanine-, BODIPY-, DPP-, Squaraine-based NIR-II Fluorophores and the Other NIR-II Organic Small Molecules

Fluorophore	Hydrophilic Modification	Targeted Modification	$\lambda_{Abs}/\lambda_{em}$ (nm)	QY[a]	Imaging Strategy	Therapeutic Mode	Biological Applications	Ref
Flav7	mPEG-DSPE	/	1,026/1,045	0.53%	FLI	/	Hindlimb imaging	Cosco et al.[118]
5H5	PEGylated	cRGDfk conjugate	1,069/1,125	0.26%	FLI	/	Blood pool, tumorous microvasculature, and tumor imaging	Ding et al.[119]
FD-1080	FBS	/	1,064/1,080	0.31%; 5.94% in serum	FLI	/	Hindlimb vasculature, abdomen, and brain vessel imaging	Li et al.[120]
FD-1080 J-aggregates	DMPC	/	1,360/1,370	0.0545%	FLI	/	Hindlimb and brain vasculature imaging, dynamic vascular imaging	Sun et al.[121]
CX-1	DSPE-mPEG$_{2k}$	/	883/920	0.66%	FLI	/	Lymphatic imaging, APAP-induced hepatotoxicity detection	Lei et al.[122]
CX-2			981/1,032	0.45%				
CX-3			1,089/1,140	0.091%				
BTC980	DOPE-mPEG	/	932/980	0.22%	FLI	/	Lymphatic imaging, ratiometric imaging, and gastric pH quantification	Wang et al.[123]
BTC982			944/982	0.30%				
BTC1070			1,014/1,070	0.016%				
IRBTP-B/ IRBTP-O	DSPE-mPEG$_{2k}$	/	575 or 905 />1,000	0.10% in methanol	Activatable FLI	/	ONOO$^-$ detection, monitoring drug-induced hepatotoxicity	Li et al.[125]
Hydro-1080/ Et-1080	/	/	1,039/1,080	0.045%	Activatable FLI	/	·OH detection, detecting hepatotoxicity caused by drug overdose	Feng et al.[126]
IR-1060/ HISSNPs	HA conjugate	/	major peak at 810, shoulder peak at 1,050/1,070	N.A.	Activatable FLI	/	Cell and tumor imaging	Tang et al.[127]
QT-RGD	/	cRGD peptides conjugate	841/1,068	0.12%	FLI/PAI/ SPECT	PTT	Multimodal imaging-guided PTT of tumor	Zhao et al.[129]
NJ960	F127	/	651 or 799/960	N.A.	FLI	/	Hindlimb, vessel, and brain imaging	Bai et al.[135]
NJ1030			668 or 830/1,030					
NJ1060			672 or 910/1,060					
SWIR-WAZABY-01	Ammonium groups onto the boron atom	/	N.A./emission between 720 and 1,200 in mouse serum	0.25% in plasma	FLI	/	Cell and tumor imaging	Godard et al.[136]
ZX-NIR/ NIRII-HS	mPEG-DSPE	/	N.A./900	N.A.	Activatable FLI	/	H$_2$S detection, cell and tumor imaging	Xu et al.[137]
BOD-M-βgal/ BOD-M-SH	/	/	N.A.	N.A.	Activatable FLI	/	βgal activatable, cell and tumor imaging	Chen et al.[138]
WD-CH$_3$	/	/	768/960	N.A.	FLI	/	Tracking the variation of viscosity in diabetes-induced liver injury	Dou et al.[139]
WD-NO$_2$			818/982	0.16% in glycerol				
WD-OCH$_3$			830/1,024	N.A.				
WD-NME$_2$			850/1,070	N.A.				
DPP-BDT	DSPE-PEG$_{5k}$	/	625/980	N.A.	FLI/PAI	PTT/PDT	Dual-modal imaging-guided PTT/PDT of tumor	Wang et al.[142]
DPP-BT	DSPE-PEG-FA	/	686/1,089	N.A.	FLI/PAI	PTT/PDT/ chemotherapy	Dual-modal imaging-guided PTT/PDT/chemo combination therapy of tumor	Wang et al.[143]

Table 3. *Continued*

Fluorophore	Hydrophilic Modification	Targeted Modification	$\lambda_{Abs}/\lambda_{em}$ (nm)	QY[a]	Imaging Strategy	Therapeutic Mode	Biological Applications	Ref
SQP J-aggregates	F-127	/	N.A./N.A. 1,100	N.A.	FLI	PTT	Vessel, brain, and body imaging; imaging-guided PTT	Sun et al.[147]
SQ1	DSPE-PEG2000	Decorated with penta-peptide CREKA	930/970	0.17%	FLI/PAI	PTT	Vessel imaging and imaging-guided PTT of tumor	Yao et al.[148]
CPTIC-4F	DSPE-mPEG	/	810 or 876/1,110	0.39% (900−1,400 nm); 0.33% (1,000−1,400 nm); 0.015% (1,300−1,400 nm)	FLI	/	Whole-body vessels imaging	Zhu et al.[149]
NDI-NA J-aggregates	DSPE-mPEG2000	/	904/1,020	0.21%	FLI	PTT/PDT	Imaging-guided PTT/PDT of tumor	Tang et al.[150]
IPIC	TPP-PEG-PPG-PEG-TPP	/	N.A.	0.22%	FLI	PTT/PDT	Imaging-guided mitochondria-targeting PTT/PDT of tumor	Wang et al.[151]
TSSI	DSPE-mPEG2000	/	N.A.	N.A.	FLI/PAI/PTI	PTT/PDT	NIR-II FLI/PAI/PTI trimodal imaging-guided PDT/PTT synergistic therapy of tumor	Zhang et al.[152]
bis-ACP	/	/	894/1,029	/	/	/	/	Lavaud et al.[153]
CSM2	F-127	/	878/N.A.	/	PAI	PTT	imaging-guided NIR-II PTT of tumor	Shao et al.[154]
Zn_4-H_2 [Pc $(OC_{12}H_{17})_{24}$]	DSPE-PEG_{2k}-OCH_3	/	1,064/N.A.	/	PAI	PTT	imaging-guided NIR-II PTT of tumor	Pan et al.[155]
IR-SS	DSPE-PEG	/	1,060/N.A.	/	PAI	PTT	imaging-guided NIR-II PTT of tumor	Li et al.[156]

[a]Fluorescence quantum yields of all small molecular NIR-II fluorophores mentioned in this review were recalculated based on IR26 = 0.05% (in 1,2-dichloroethane).

First, 2-aminoethanethiol was used to link the hydrophilic hyaluronic acid (HA) and hydrophobic NIR-II fluorophore **IR-1061**. The single-factor response probe (HINPs) was developed through self-assembly. Then, HA was cross-linked by disulfide bond to form the dual-factor responsive probe HISSNPs. HA could not only specifically bind to glycoprotein on the surface of CD44 overexpressed tumor cells, but cooperate with disulfide to lock **IR-1061**. The locked fluorophores were in the aggregated states, resulting in the NIR-II fluorescence quenching. In the tumor microenvironment with overexpression of hyaluronidase and thiols, **IR-1061** was released on-site to emit its NIR-II fluorescence. In the tumor-bearing mice model, HISSNPs presented a lower background, higher tumor-to-normal tissue ratio (15.4/3.3), as well as a higher tumor-to-liver ratio (5.87/1.1) than HINPs. HISSNPs significantly improved the imaging quality and more accurately distinguished normal tissues from diseased tissues.

Some integrated diagnostic and therapeutic cyanine-based NIR-II agents have also been developed. The macromolecular **PF** was prepared via conjugating NIR-II fluorophore **Flav7** with an amphiphilic polypeptide.[128] Through self-assembly, **PF** could form the water-soluble NPs by itself. Through the EPR effect and endothelial leakiness, **PF** NPs could effectively accumulate at the tumor site. Due to the good photothermal property of **Flav7**, the stable **PF** NPs presented a photothermal conversion efficiency of 42.3% under the 808-nm laser irradiation. The location, size, and ablation of the tumor could be clearly visualized through NIR-II FLI.

In addition to passive accumulation at the tumor sites via the EPR effect, another NIR-II probe **QT-RGD** with active tumor-targeting property was prepared by conjugating a [125] I-modified NIR-II cyanine fluorophore and two cRGD peptides (Figure 5B).[129] Due to the cRGD peptides, the probe could specifically bind to $\alpha_v\beta_3$ integrin for active tumor-targeting. Under the NIR laser irradiation, the probe was capable of three-mode NIR-II fluorescence imaging, PAI, and single-photon emission computed tomography (SPECT) imaging.

Moreover, the good photothermal conversion efficiency (36.5%) enabled it as an excellent photothermal agent to ablate the tumors under 808 nm photoirradiation. This targeted probe integrates multiple imaging methods and phototherapy, which dramatically improves the accuracy of tumor diagnosis and the efficiency of cancer treatment.

BODIPY/aza-BODIPY-based NIR-II Fluorophores

Dipyrromethene boron difluoride (BODIPY)-derived fluorophores are widely used in the fields of NIR-I imaging and phototherapy due to the advantages of excellent chemical/photostability, high molar extinction coefficient, and low toxicity.[130–133] As a typical derivative of BODIPY, Aza-BODIPY has more prolonged absorption and emission wavelengths due to the replacement of the carbon atom at the meso-position by a nitrogen atom, resulting in pronounced red-shift.[134] Recently, some NIR-II fluorophores based on BODIPY/Aza-BODIPY have been developed (Table 1).

Bai et al. developed three Aza-BODIPY-based NIR-II fluorophores **NJ960**, **NJ1030**, and **NJ1060** via D-A-D strategy.[135] Corresponding NPs of these novel fluorophores presented a large Stokes shift, excellent brightness, and superior photostability. These new Aza-BODIPY-based NIR-II fluorophores provided an excellent platform to further construct NIR-II fluorescent probes with better water solubility, higher fluorescence QY, and more extended NIR-II emission for clinical applications. Very recently, another water-soluble Aza-BODIPY **SWIR-WAZABY-01** with a fluorescence tail into the NIR-II region was reported by Godard et al.[136] Although this is the first report of NIR-II water-soluble aza-BODIPY fluorophore, the introduction of ammonium groups caused the blue-shift of the original fluorophore, making the NIR-II emission not perfect.

The "turn-on" type fluorophores have many advantages, such as high target-to-background ratio and excellent specificity. However, the development of such fluorophores is still challenging. Besides the Cyanine-based
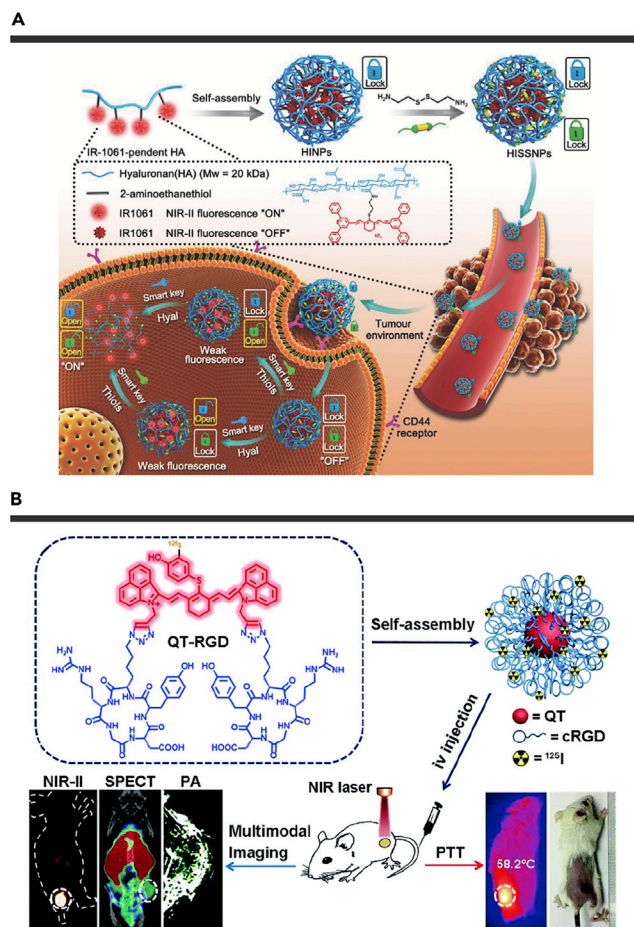
Figure 5. Fluorescence Activation Process and Multimodal Imaging of Small Molecular NIR-II Fluorophores (A) Synthesis of "lock-and-key"-controlled tumor-specific imaging nanoparticles (HISSNPs) and its NIR-II fluorescence activation process. Reproduced with permission from Tang et al.[127] Copyright 2018 Wiley-VCH. (B) Self-assembly of **QT-RGD** and its applications in trimodal imaging and PTT of tumors *in vivo*. Reproduced with permission from Zhao et al.[129] Copyright 2020 Royal Society of Chemistry.

"turn-on" fluorophores, BODIPY-based "turn-on" NIR-II probes have also been exploited. For example, an H2S-activatable nanoprobe was prepared by encapsulating an H2S-responsive fluorophore **ZX-NIR** and an H2S-inert fluorophore aza-BOD with DSPE-*m*PEG and TBNBr.[137] The fluorophore **ZX-NIR** could generate NIR-II fluorescence only when activated by H2S (Table 1). Another fluorophore aza-BOD acted as the internal reference to enable the nanoprobe to emit multiple wavelengths for ratiometric imaging. *In vivo* studies on animal models demonstrated that such water-soluble, biocompatible, and fast-responsive nanoprobe could accurately image and diagnose colorectal tumors with rich H2S. Another enzyme-activated probe **BOD-M-βgal** was prepared by employing a self-disappearing unit to link β-galactosidase (β-Gal) residues and BODIPY-based fluorophore (Table 1).[138] Under the β-Gal activation, **BOD-M-βgal** showed an NIR-II emission range from 900 nm to 1,300 nm. The β-Gal-rich ovarian tumors could be quickly and accurately detected upon the NIR-II fluorescence imaging of this probe.

Besides the H2S-activatable and β-Gal-activatable probes, a series of viscosity-activatable NIR-II fluorophores were developed by introducing different substituents onto the BODIPY-based platform.[139] Among them, **WD-NO₂** showed a relatively high fluorescence QY of 0.16% in glycerol, and it was very sensitive to viscosity variations but not sensitive to some other environmental factors, such as pH and polarity (Table 1). With the increase of environmental viscosity, the fluorescence intensity of **WD-NO₂** presented a 31-fold enhancement. Due to these characteristics, **WD-NO₂** was used to

track the diabetes-induced liver injury process-related viscosity variations *in vivo*.

DPP-based NIR-II Fluorophores

DPP with planar lactam structure is a common electron-acceptor.[140] Due to the existence of multiple reaction sites on the DPP segment, various DPP derivatives have been exploited with the advantages of high fluorescence QY, tunable photophysical properties, excellent thermal/photostability, and low dark toxicity.[141] However, DPP-based NIR-II small molecular fluorophores are still very rare (Table 1).

In 2019, Wang et al. reported a multifunctional NIR-II fluorophore **DPP-BDT**.[142] The water-soluble and biocompatible **DPP-BDT** NPs were prepared via nanoprecipitation and showed good photostability. The maximum absorption and emission peak of **DPP-BDT** NPs were 625 nm and 980 nm, respectively. Under the 660 nm laser irradiation, **DPP-BDT** NPs exhibited a photothermal conversion efficiency of 23% and a $^1O_2$ QY of ~49.3%. *In vitro* and *in vivo* studies confirmed that these NPs had a high tumor treatment efficacy, benefiting from the combination of PTT and PDT under NIR-II fluorescence/photoacoustic dual-modal imaging navigation (Figure 6A).

In the same year, another multifunctional NIR-II fluorophore **DPP-BT** was reported.[143] **DPP-BT** NPs with an absorption peak at 686 nm and emission peak at 1,089 nm could not only be capable of NIR-II fluorescence/photoacoustic dual-modal imaging but also both had photodynamic and photothermal properties. Under the 730-nm laser irradiation, **DPP-BT** NPs presented a $^1O_2$ QY of ~27.3% and high photothermal conversion efficiency of 50%. To further integrate chemotherapy, the single NIR laser triggered phototheranostic platform P(DPP-BT/DOX) NPs was developed via encapsulating **DPP-BT**, chemo-drug doxorubicin (DOX), and natural phase-change materials with the folic acid-modified amphiphilic polymer matrix and lecithin. Due to the combination of photothermal/photodynamic and chemotherapy, the single laser triggered NPs presented unprecedented anti-tumor performance (Figure 6B). This work provides an innovative way to design and construct multimodal diagnosis and treatment-integrated nanoplatforms for clinical cancer therapy.

Squaraine-based NIR-II Fluorophores

Squaraine dyes are a type of zwitterionic molecules featured with a unique four-membered ring π-conjugated skeleton derived from squaric acid. They are widely employed to construct fluorophores due to their intensive fluorescence and easily tunable bandgap.[144] Especially, it can form *J*-aggregates via nanoprecipitation, which will cause red-shift or brightness enhancement[145,146]; however, the development of squaraines with long emission is still challenging (Table 1).

In 2018, Sun et al. reported a squaraine-based fluorophore **SQP**.[147] The *J*-aggregated **SQP**-NPs(J) were prepared by encapsulating **SQP** into amphiphilic F127, showing high brightness with an emission peak of ~1,100 nm. Compared with the *H*-aggregated **SQP**-NPs(H), the emission intensity of **SQP**-NPs(J) presented a 4.8-fold enhancement. **SQP**-NPs(J) presented a photothermal conversion efficiency of 36% under the LED lamp irradiation and was then used for NIR-II fluorescence imaging-guided PTT of MCF-7 tumor-bearing mice.

Based on the common squaraine, another squaraine-based D-A-D structured fluorophore **SQ1** was synthesized by introducing a powerful electron-withdrawing unit, malononitrile, to improve the electron affinity, resulting in a strong ICT and a pronounced red-shift.[148] As a result, the fluorescence spectrum of **SQ1** reached the NIR-II region, with an absorption and emission peak at 930 nm and 970 nm, respectively. **SQ1** NPs were prepared via nanoprecipitation and were then decorated with an active-targeting ligand peptide CREKA to form **SQ1** nanoprobe (Figure 6C). After being coated with the amphiphilic polymer, fluorescence QY of **SQ1** could be increased from 0.013% to 0.17%, which was attributed to the formation of *J*-aggregates in the hydrophobic interior of the polymer by **SQ1** molecules. With the targeted peptide, the nanoprobe could specifically target fibronectin overexpressed in breast cancer. Under NIR-II fluorescence and photoacoustic dual-modal imaging, breast cancer and lung metastasis could be accurately detected.
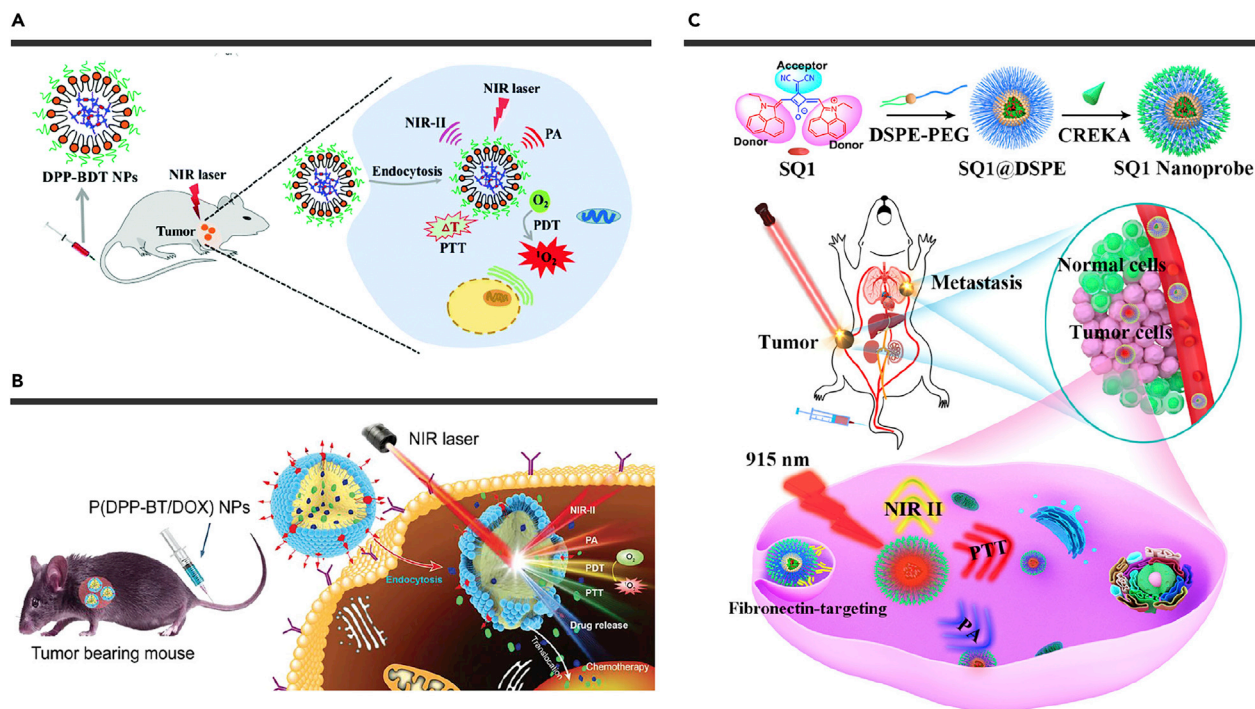
Figure 6. Integrated Diagnosis and Treatment of Small Molecular NIR-II Fluorophores (A) Applications of **DPP-BDT** NPs in NIR-II fluorescence/photoacoustic imaging-guided cancer PDT/PTT. Reproduced with permission from Wang et al.[142] Copyright 2019 Royal Society of Chemistry. (B) Applications of P(**DPP-BT**/DOX) NPs in NIR-II fluorescence/photoacoustic dual-modal imaging-guided cancer PDT/PTT/Chemotherapy. Reproduced with permission from Wang et al.[143] Copyright 2019 Wiley-VCH. (C) Synthetic schematic diagram of **SQ1** nanoprobe for NIR-II fluorescence/photoacoustic dual-modal imaging-guided PTT of metastatic breast cancer. Reproduced with permission from Yao et al.[148] Copyright 2020 American Chemical Society.

Under the 915-nm laser irradiation, **SQ1** nanoprobe with a photothermal conversion efficiency of 25.6% had hyperthermia effects on tumors.

Other NIR-II Organic Small Molecules

In the past few years, small molecular NIR-II fluorophores have entered a new stage with rapid development. In addition to expanding the library of original fluorophores, it is still necessary to further exploit new types of NIR-II small molecular fluorophores (Table 1). Very recently, a bright fused-ring acceptor based NIR-II molecule **CPTIC-4F** has been reported.[149] **CPTIC-4F** NPs presented an emission peak at 1,110 nm with a fluorescence QY of 0.39% and a high absorption coefficient of 14.5×10^4 $M^{-1} \cdot cm^{-1}$. Another novel naphthalenediimide-based polycyclic fluorophore **NDI-NA** could form J-aggregates via nanoprecipitation, which caused a pronounced red-shift in both absorption and emission.[150] Besides, **NDI-NA** NPs presented a photothermal conversion efficiency of 30.8%.

Moreover, a "one-for-all" probe by self-assembly of NIR-II molecule **IPIC** and triphenylphosphonium (TPP) modified amphiphilic polymer (TPP-PEG-PPG-PEG-TPP) was reported, the TPP group endowed the probe mitochondrial targeting property.[151] Under the 808-nm laser irradiation, the probe showed fluorescence QY of 0.22% in aqueous solution and photothermal conversion efficiency of 39.6%. Meanwhile, it had singlet oxygen QY of 2.3%, which was approximately 12-fold higher than that of ICG. Recently, Zhang et al. also reported a "one-for-all" NIR-II AIEgen **TSSI** through the introduction of a new electron-acceptor of 1,3-bis(dicyanomethylidene)indane moiety for extremely strong ICT.[152] With a balance between non-radiative and radiative transitions, **TSSI** NPs presented a high photothermal conversion efficiency of 46% and acceptable NIR-II fluorescence. Interestingly, **TSSI** NPs could generate ·OH, which suggested it could be used as a type I photosensitizer for PDT. And **TSSI** NPs succeeded in NIR-II fluorescence/photoacoustic/photothermal trimodal imaging-guided synergistic PDT/PTT. As brought up new viewpoints in the molecular design of multifunctional NIR-II fluorophores for tumor phototheranostics.

Up to now, many NIR-II fluorophores have been successfully used for phototheranostics; nevertheless, their absorption wavelength is mainly limited to the NIR-I region, which impedes the phototherapeutic efficacy of deep-seated tumors. Recently, several small molecules with NIR-II absorption, such as **bis-ACP**, **CSM2**, and **Zn_4-H_2[Pc(OC$_{12}$H$_{17}$)$_{24}$]**, have been reported to accomplish PAI-guided NIR-II PTT (Table 1).[153−155] Among them, phthalocyanine-derived **Zn_4-H_2[Pc(OC$_{12}$H$_{17}$)$_{24}$]** showed a high photothermal conversion efficiency of 58.3% under the 1,064-nm laser irradiation. Though these molecules had been successfully applied for NIR-II PTT, the photothermal conversion efficiency still needed to be improved. Very recently, an NIR-II photothermal agent **IR-SS** was developed via Se-tailoring strategy.[156] By introducing two Se atoms into the BBT acceptor skeleton, a pronounced red-shift in absorption could be observed. **IR-SS** NPs presented an unprecedented high photothermal conversion efficiency of 77% under the 1,064-nm laser irradiation. This work opens a new insight into the design and development of high-performance NIR-II photothermal agents.

CONCLUSION AND OUTLOOK

Herein, we have systematically reviewed the recent advances in the preparation and application of organic small molecular NIR-II fluorophores and classified them based on the electron-withdrawing cores. NIR-II small molecular fluorophores with the advantages of good biocompatibility, structural adjustment, and excellent photophysical properties have been widely used in the biomedical field, such as bioimaging, surgical navigation, and imaging-guided phototherapy. Due to the high resolution, good SBR, and excellent lesion recognition ability, NIR-II FLI can accurately and real-time visualize various physiological and pathological processes. Significantly, the tumors can be removed more thoroughly and precisely by NIR-II FLI-guided surgery. The integration of NIR-II FLI and phototherapy has greatly further improved the therapeutic efficiency and accuracy of cancer treatment.

In addition to the existing success, the future development and application of NIR-II small molecular fluorophores still face some challenges in the following aspects.

Improving NIR-II Fluorescence Imaging Quality

Improving imaging quality usually revolves around the optimization of the fluorescence wavelength, fluorescence QY, and fluorescence brightness. At present, most strategies focus on improving the fluorescence QY to improve brightness, such as the construction of S-D-A-D-S structure or self-assembly with serum. The absorption coefficient is also the other factor for brightness optimization. Exploiting fluorophore molecules with both high fluorescence QY and the high absorption coefficient is still a challenge. Recently, NIR-IIa and NIR-IIb fluorescence imaging have greatly improved the imaging depth. However, fluorophores with such characteristics are still in their infancy. Thus, the development of fluorophores with great stability, high brightness, and long absorption/emission wavelength is still an important research direction in the future.

Exploiting Targeted, Activatable, and Multifunctional NIR-II Fluorophores

Currently, most NIR-II fluorophores passively accumulate at the tumor site via the EPR effect. However, this passive targeting way often results in a certain accumulation of fluorophores in normal tissues, which will cause poor target-to-background ratio or even false positive. Thus, the development of active-targeting and activatable probes is of great significance to accurately distinguish diseased tissues from normal tissues. To improve the efficiency of tumor treatment, it is also urgent to develop various probes with integrated diagnostic and therapeutic performance. At present, most multifunctional probes are used for imaging-guided PTT of tumors, and chemotherapy is still the main way for clinical cancer treatment. Therefore, the combination of NIR-II fluorescence imaging with photodynamic therapy, chemotherapy, or vascular-disruption therapy is of great importance to further improve the efficiency of cancer treatment. In our point of view, this is also a potential research direction with considerable research value.

Overcoming the BBB

The diagnosis and treatment of brain tumors have always been a difficult problem in biomedicine. This is mainly because the dense BBB can effectively block the penetration of contrast agents or probes. However, in current reports, NIR-II small molecular probes that can effectively cross the BBB are relatively rare. Thus, the development of NIR-II probes with BBB-crossing capability is of great significance for the diagnosis and treatment of brain tumors.

Accelerating Clinical Translation

Based on the FDA-approved ICG, NIR-II fluorescence imaging has been used in clinical surgical navigation. However, low fluorescence QY and poor fluorescence intensity of the traditional NIR-I fluorophore in the NIR-II region limit the clinical performance of NIR-II fluorescence imaging. The rapid excretion and nontoxic features of ICG are the key to its clinical translation. Unfortunately, none of the currently developed NIR-II fluorophores can well balance various properties to meet the requirement of the FDA. That is the main reason why no NIR-II fluorophore has been approved by the FDA for clinical application, as is also a huge challenge in the future. Accelerating the clinical translation of NIR-II fluorophores still has a long way to go.

REFERENCES

1. Yang, Z., and Chen, X. (2019). Semiconducting perylene diimide nanostructure: multifunctional phototheranostic nanoplatform. Acc. Chem. Res. **52**, 1245–1254.
2. Chen, C., Ou, H., Liu, R., et al. (2020). Regulating the photophysical property of organic/polymer optical agents for promoted cancer phototheranostics. Adv. Mater. **32**, 1806331.
3. Li, J., Zhen, X., Lyu, Y., et al. (2018). Cell membrane coated semiconducting polymer nanoparticles for enhanced multimodal cancer phototheranostics. ACS. Nano. **12**, 8520–8530.
4. Li, J., and Pu, K. (2019). Development of organic semiconducting materials for deep-tissue optical imaging, phototherapy and photoactivation. Chem. Soc. Rev. **48**, 38–71.
5. Saba, L., Sanfilippo, R., Montisci, R., et al. (2010). Carotid artery wall thickness: comparison between sonography and multi-detector row CT angiography. Neuroradiology **52**, 75–82.
6. Takami, Y., Norikane, T., Yamamoto, Y., et al. (2020). A preliminary study of relationship among the degree of internal carotid artery stenosis, wall shear stress on MR angiography and ^{18}F-FDG uptake on PET/CT. J. Nucl. Cardiol. https://doi.org/10.1007/s12350-020-02300-3.
7. Wang, D., Li, Z., Zheng, X., et al. (2020). Head and neck CT angiography to assess the internal carotid artery stealing pathway. BMC. Neurol. **20**, 334.
8. Pichler, B.J., Kolb, A., Nagele, T., et al. (2010). PET/MRI: paving the way for the next generation of clinical multimodality imaging applications. J. Nucl. Med. **51**, 333–336.
9. Zhang, Y., Garcia-Gabilondo, M., Grayston, A., et al. (2020). PLGA protein nanocarriers with tailor-made fluorescence/MRI/PET imaging modalities. Nanoscale **12**, 4988–5002.
10. Rischpler, C., Siebermair, J., Kessler, L., et al. (2020). Cardiac PET/MRI: current clinical status and future perspectives. Semin. Nucl. Med. **50**, 260–269.
11. Bezukladova, S., Tuisku, J., Matilainen, M., et al. (2020). Insights into disseminated MS brain pathology with multimodal diffusion tensor and PET imaging. Neurol. Neuroimmunol. Neuroinflamm. **7**, 691.
12. Ming, Y., Wu, N., Qian, T., et al. (2020). Progress and future trends in PET/CT and PET/MRI molecular imaging approaches for breast cancer. Front. Oncol. **10**, 1301.
13. Dimitrakopoulou-Strauss, A., Pan, L., and Sachpekidis, C. (2020). Kinetic modeling and parametric imaging with dynamic PET for oncological applications: general considerations, current clinical applications, and future perspectives. Eur. J. Nucl. Med. Mol. Imaging. https://doi.org/10.1007/s00259-020-04843-6.
14. Miao, Q., and Pu, K. (2018). Organic semiconducting agents for deep-tissue molecular imaging: second near-infrared fluorescence, self-luminescence, and photoacoustics. Adv. Mater. **30**, 1801778.
15. Huang, J., Xie, C., Zhang, X., et al. (2019). Renal-clearable molecular semiconductor for second near-infrared fluorescence imaging of kidney dysfunction. Angew. Chem. Int. Ed. **58**, 15120.
16. Tu, L., Xu, Y., Ouyang, Q., et al. (2019). Recent advances on small-molecule fluorophores with emission beyond 1000 nm for better molecular imaging in vivo. Chin. Chem. Lett. **30**, 1731–1737.
17. Zhang, F., and Lei, Z. (2020). Molecular engineering of NIR-II fluorophores for improved biomedical detection. Angew. Chem. Int. Ed. https://doi.org/10.1002/anie.202007040.
18. Li, C., Chen, G., Zhang, Y., et al. (2020). Advanced fluorescence imaging technology in the near-infrared-II window for biomedical applications. J. Am. Chem. Soc. **142**, 14789–14804.
19. Zhu, S., Yung, B.C., Chandra, S., et al. (2018). Near-infrared-II (NIR-II) bioimaging via off-peak NIR-I fluorescence emission. Theranostics **8**, 4141–4151.
20. Cao, J., Zhu, B., Zheng, K., et al. (2019). Recent progress in NIR-II contrast agent for biological imaging. Front. Bioeng. Biotechnol. **7**, 487.
21. Huang, J., and Pu, K. (2020). Activatable molecular probes for second near-infrared fluorescence, chemiluminescence, and photoacoustic imaging. Angew. Chem. Int. Ed. **59**, 11717.
22. Wan, H., Du, H., Wang, F., et al. (2019). Molecular imaging in the second near-infrared window. Adv. Funct. Mater. **29**, 1900566.
23. He, S., Song, J., Qu, J., et al. (2018). Crucial breakthrough of second near-infrared biological window fluorophores: design and synthesis toward multimodal imaging and theranostics. Chem. Soc. Rev. **47**, 4258–4278.
24. Hu, Z., Fang, C., Li, B., et al. (2020). First-in-human liver-tumour surgery guided by multispectral fluorescence imaging in the visible and near-infrared-I/II windows. Nat. Biomed. Eng. **4**, 259–271.
25. Wang, C., Wang, Z., Zhao, T., et al. (2018). Optical molecular imaging for tumor detection and image-guided surgery. Biomaterials **157**, 62–75.
26. Sorolla, M.A., Parisi, E., and Sorolla, A. (2020). Determinants of sensitivity to radiotherapy in endometrial cancer. Cancers **12**, 1906.
27. Sun, B., Luo, C., Cui, W., et al. (2017). Chemotherapy agent-unsaturated fatty acid prodrugs and prodrug-nanoplatforms for cancer chemotherapy. J. Control Release. **264**, 145–159.
28. De Ruysscher, D., Niedermann, G., Burnet, N.G., et al. (2019). Radiotherapy toxicity. Nat. Rev. Dis. Primers **5**, 13.
29. Cai, Y., Wei, Z., Song, C., et al. (2019). Optical nano-agents in the second near-infrared window for biomedical applications. Chem. Soc. Rev. **48**, 22–37.
30. Yang, N., Xiao, W., Song, X., et al. (2020). Recent advances in tumor microenvironment hydrogen peroxide-responsive materials for cancer photodynamic therapy. Nano-micro Lett. **12**, 15.
31. Xie, Z., Fan, T., An, J., et al. (2020). Emerging combination strategies with phototherapy in cancer nanomedicine. Chem. Soc. Rev. **49**, 8065–8087.
32. Liang, P., Huang, X., Wang, Y., et al. (2018). Tumor-microenvironment-responsive nanoconjugate for synergistic antivascular activity and phototherapy. ACS. Nano **12**, 11446–11457.
33. Teng, L., Song, G., Liu, Y., et al. (2019). Nitric oxide-activated "dual-key-one-lock" nanoprobe for in vivo molecular imaging and high-specificity cancer therapy. J. Am. Chem. Soc. **141**, 13572–13581.

34. Zou, J., Zhu, J., Yang, Z., et al. (2020). A phototheranostic strategy to continuously deliver singlet oxygen in the dark and hypoxic tumor microenvironment. Angew. Chem. Int. Ed. **59**, 8833–8838.

35. Jia, J., Liu, G., Xu, W., et al. (2020). Fine-tuning the homometallic interface of Au-on-Au nanorods and their photothermal therapy in the NIR-II window. Angew. Chem. Int. Ed. **59**, 14443–14448.

36. Cai, Y., Si, W., Huang, W., et al. (2018). Organic dye based nanoparticles for cancer phototheranostics. Small **14**, 1704247.

37. Wang, Y.Y., Liu, Y.C., Sun, H., et al. (2019). Type I photodynamic therapy by organic-inorganic hybrid materials: from strategies to applications. Coord. Chem. Rev. **395**, 46–62.

38. Li, X., Kwon, N., Guo, T., et al. (2018). Innovative strategies for hypoxic-tumor photodynamic therapy. Angew. Chem. Int. Ed. **57**, 11522.

39. Chen, D., Wang, Z., Dai, H., et al. (2020). Boosting $O_2^{\bullet-}$ photogeneration via promoting intersystem-crossing and electron-donating efficiency of aza-BODIPY-based nanoplatforms for hypoxic-tumor photodynamic therapy. Small. Methods **4**, 2000013.

40. Chen, D., Yu, Q., Huang, X., et al. (2020). A highly-efficient Type I photosensitizer with robust vascular-disruption activity for hypoxic-and-metastatic tumor specific photodynamic therapy. Small **16**, 2001059.

41. Welsher, K., Sherlock, S.P., and Dai, H. (2011). Deep-tissue anatomical imaging of mice using carbon nanotube fluorophores in the second near-infrared window. Proc. Natl. Acad. Sci. U S A **108**, 8943–8948.

42. Mandal, A.K., Wu, X., Ferreira, J.S., et al. (2020). Fluorescent sp$^{(3)}$ defect-tailored carbon nanotubes enable NIR-II single particle imaging in live brain slices at ultra-low excitation doses. Sci. Rep. **10**, 5286.

43. Hong, G., Lee, J.C., Robinson, J.T., et al. (2012). Multifunctional in vivo vascular imaging using near-infrared II fluorescence. Nat. Med. **18**, 1841–1846.

44. Zhang, J.J., Lin, Y., Zhou, H., et al. (2019). Cell membrane-camouflaged NIR-II fluorescent Ag$_2$Te quantum dots-based nanobioprobes for enhanced in vivo homotypic tumor imaging. Adv. Healthc. Mater. **8**, 1900341.

45. He, H., Lin, Y., Tian, Z.Q., et al. (2018). Ultrasmall Pb: Ag$_2$S quantum dots with uniform particle size and bright tunable fluorescence in the NIR-II window. Small **14**, 1703296.

46. Zebibula, A., Alifu, N., Xia, L., et al. (2018). Ultrastable and biocompatible NIR-II quantum dots for functional bioimaging. Adv. Funct. Mater. **28**, 1703451.

47. Zhong, Y., Ma, Z., Wang, F., et al. (2019). In vivo molecular imaging for immunotherapy using ultra-bright near-infrared-IIb rare-earth nanoparticles. Nat. Biotechnol. **37**, 1322–1331.

48. Zhang, X., He, S., Ding, B., et al. (2020). Cancer cell membrane-coated rare earth doped nanoparticles for tumor surgery navigation in NIR-II imaging window. Chem. Eng. J. **385**, 123959.

49. Li, X., Jiang, M., Li, Y., et al. (2019). 808nm laser-triggered NIR-II emissive rare-earth nanoprobes for small tumor detection and blood vessel imaging. Mater. Sci. Eng. C **100**, 260–268.

50. Liu, S., Ou, H., Li, Y., et al. (2020). Planar and twisted molecular structure leads to the high brightness of semiconducting polymer nanoparticles for NIR-IIa fluorescence imaging. J. Am. Chem. Soc. **142**, 15146–15156.

51. Jiang, Y., Upputuri, P.K., Xie, C., et al. (2019). Metabolizable semiconducting polymer nanoparticles for second near-infrared photoacoustic imaging. Adv. Mater. **31**, 1808166.

52. Liu, G., Zhu, J., Guo, H., et al. (2019). Mo$_2$C-derived polyoxometalate for NIR-II photoacoustic imaging-guided chemodynamic/photothermal synergistic therapy. Angew. Chem. Int. Ed. **58**, 18641–18646.

53. Wen, G., Li, X., Zhang, Y., et al. (2020). Effective phototheranostics of brain tumor assisted by near-infrared-II light-responsive semiconducting polymer nanoparticles. ACS. Appl. Mater. Interfaces **12**, 33492–33499.

54. Yang, Y., Fan, X., Li, L., et al. (2020). Semiconducting polymer nanoparticles as theranostic system for near-Infrared-II fluorescence imaging and photothermal therapy under safe laser fluence. ACS. Nano **14**, 2509–2521.

55. Liu, Y., Liu, J., Chen, D., et al. (2020). Fluorination enhances NIR-II fluorescence of polymer dots for quantitative brain tumor imaging. Angew. Chem. Int. Ed. **59**, 21049.

56. Li, J., Liu, Y., Xu, Y., et al. (2020). Recent advances in the development of NIR-II organic emitters for biomedicine. Coord. Chem. Rev. **415**, 213318.

57. Shao, J., Guo, X., Shi, N., et al. (2018). Acenaphthylene-imide based small molecules/ TiO$_2$ bilayer as electron-transporting layer for solution-processing efficient perovskite solar cells. Sci. China Mater. **62**, 497–507.

58. Wang, W., Yang, Q., Du, Y., et al. (2020). Metabolic labeling of peptidoglycan with NIR-II dye enables in vivo imaging of gut microbiota. Angew. Chem. Int. Ed. **59**, 2628.

59. Li, L., Dong, X., Li, J., et al. (2020). A short review on NIR-II organic small molecule dyes. Dyes Pigm. **183**, 108756.

60. Zhang, X., An, L., Tian, Q., et al. (2020). Tumor microenvironment-activated NIR-II reagents for tumor imaging and therapy. J. Mater. Chem. B **8**, 4738–4747.

61. Fang, Y., Shang, J., Liu, D., et al. (2020). Design, synthesis, and application of a small molecular NIR-II fluorophore with maximal emission beyond 1200 nm. J. Am. Chem. Soc. **142**, 15271–15275.

62. Li, Y., Hu, D., Sheng, Z., et al. (2020). Self-assembled AIEgen nanoparticles for multiscale NIR-II vascular imaging. Biomaterials **264**, 120365.

63. Liu, M.H., Zhang, Z., Yang, Y.C., et al. (2020). Polymethine-based semiconducting polymer dots with narrow-band emission and absorption/emission maxima at NIR-II for bioimaging. Angew. Chem. Int. Ed. https://doi.org/10.1002/anie.202011914.

64. Qi, J., Alifu, N., Zebibula, A., et al. (2020). Highly stable and bright AIE dots for NIR-II deciphering of living rats. Nano Today **34**, 100893.

65. Shao, J., Wang, G., Wang, K., et al. (2015). Direct arylation polycondensation for efficient synthesis of narrow-bandgap alternating D-A copolymers consisting of naphthalene diimide as an acceptor. Polym. Chem. **6**, 6836–6844.

66. Ren, T.B., Wang, Z.Y., Xiang, Z., et al. (2020). A general strategy for development of activatable NIR-II fluorescent probes for in vivo high-contrast bioimaging. Angew. Chem. Int. Ed. https://doi.org/10.1002/anie.202009986.

67. Xu, W., Wang, D., and Tang, B.Z. (2020). NIR-II AIEgens: a win-win integration towards bioapplications. Angew. Chem. Int. Ed. https://doi.org/10.1002/anie.202005899.

68. Xie, Y., and Li, Z. (2020). Approaching aggregated state chemistry accelerated by aggregation-induced emission. Natl. Sci. Rev. https://doi.org/10.1093/nsr/nwaa199.

69. Gangemi, C.M.A., Puglisi, R., Pappalardo, A., et al. (2018). Supramolecular complexes for nanomedicine. Bioorg. Med. Chem. Lett. **28**, 3290–3301.

70. Song, X., Zhu, W., Ge, X., et al. (2020). Engineering the protein corona structure on gold nanoclusters enables red-shifted emissions in the second near-infrared window for gastrointestinal imaging. Angew. Chem. Int. Ed. https://doi.org/10.1002/anie.202010870.

71. Wu, Y., Wang, C., Guo, J., et al. (2020). An RGD modified water-soluble fluorophore probe for in vivo NIR-II imaging of thrombosis. Biomater. Sci. **8**, 4438–4446.

72. Song, X., Zhu, W., Ge, X., et al. (2020). A new class of NIR-II gold nanoclusters based protein biolabels for in vivo tumor-targeted imaging. Angew. Chem. Int. Ed. https://doi.org/10.1002/anie.202010870.

73. Feng, G., Zhang, G.Q., and Ding, D. (2020). Design of superior phototheranostic agents guided by jablonski diagrams. Chem. Soc. Rev. **49**, 8179–8234.

74. Wang, W., Ma, Z., Zhu, S., et al. (2018). Molecular cancer imaging in the second near-infrared window using a renal-excreted NIR-II fluorophore-peptide probe. Adv. Mater. **30**, 1800106.

75. Ono, K., Tanaka, S., and Yamashita, Y. (1994). Benzobis(thiadiazole)s containing hypervalent sulfur atoms: novel heterocycles with high electron affinity and short intermolecular contacts between heteroatoms. Angew. Chem. Int. Ed. **33**, 1977–1979.

76. Qian, G., Dai, B., Luo, M., et al. (2008). Band gap tunable, donor-acceptor-donor charge-transfer heteroquinoid-based chromophores: near infrared photoluminescence and electroluminescence. Chem. Mater. **20**, 6208–6216.

77. Wang, B., Feng, G., Seifrid, M., et al. (2016). Antibacterial narrow-band-gap conjugated oligoelectrolytes with high photothermal conversion efficiency. Angew. Chem. Int. Ed. **56**, 16063–16066.

78. Yuen, J.D., Wang, M., Fan, J., et al. (2015). Importance of unpaired electrons in organic electronics. J. Polym. Sci. A Polym. Chem. **53**, 287–293.

79. Liu, Y., Phan, H., Herng, T.S., et al. (2017). Toward benzobis(thiadiazole)-based diradicaloids. Chem. Asian J. **12**, 2177–2182.

80. Ye, F., Chen, W., Pan, Y., et al. (2019). Benzobisthiadiazoles: from structure to function. Dyes Pigm. **171**, 107746.

81. Zhou, B., Hu, Z., Jiang, Y., et al. (2018). Theoretical exploitation of acceptors based on benzobis(thiadiazole) and derivatives for organic NIR-II fluorophores. Phys. Chem. Chem. Phys. **20**, 19759–19767.

82. Antaris, A.L., Chen, H., Cheng, K., et al. (2016). A small-molecule dye for NIR-II imaging. Nat. Mater. **15**, 235–242.

83. Sun, Y., Qu, C., Chen, H., et al. (2016). Novel benzo-bis(1,2,5-thiadiazole) fluorophores for in vivo NIR-II imaging of cancer. Chem. Sci. **7**, 6203–6207.

84. Sun, Y., Ding, M., Zeng, X., et al. (2017). Novel bright-emission small-molecule NIR-II fluorophores for in vivo tumor imaging and image-guided surgery. Chem. Sci. **8**, 3489–3493.

85. Zeng, X., Xue, L., Chen, D., et al. (2019). A bright NIR-II fluorescent probe for breast carcinoma imaging and image-guided surgery. Chem. Commun. **55**, 14287–14290.

86. Zhang, X.D., Wang, H., Antaris, A.L., et al. (2016). Traumatic brain injury imaging in the second near-infrared window with a molecular fluorophore. Adv. Mater. **28**, 6872–6879.

87. Wan, H., Ma, H., Zhu, S., et al. (2018). Developing a bright NIR-II fluorophore with fast renal excretion and its application in molecular imaging of immune checkpoint PD-L1. Adv. Funct. Mater. **28**, 1804956.

88. Zhu, S., Yang, Q., Antaris, A.L., et al. (2019). Molecular imaging of biological systems with a clickable dye in the broad 800- to 1,700-nm near-infrared window. Proc. Natl. Acad. Sci. U S A **114**, 962–967.

89. Yang, Q., Ma, Z., Wang, H., et al. (2017). Rational design of molecular fluorophores for biological imaging in the NIR-II window. Adv. Mater. **29**, 1605497.

90. Yang, Q., Hu, Z., Zhu, S., et al. (2018). Donor engineering for NIR-II molecular fluorophores with enhanced fluorescent performance. J. Am. Chem. Soc. **140**, 1715–1724.

91. Ma, H., Liu, C., Hu, Z., et al. (2020). Propylenedioxy thiophene donor to achieve NIR-II molecular fluorophores with enhanced brightness. Chem. Mater. **32**, 2061–2069.

92. Antaris, A.L., Chen, H., Diao, S., et al. (2017). A high quantum yield molecule-protein complex fluorophore for near-infrared II imaging. Nat. Commun. **8**, 15269.

93. Zeng, X., Xiao, Y., Lin, J., et al. (2018). Near-infrared II dye-protein complex for biomedical imaging and imaging-guided photothermal therapy. Adv. Healthc. Mater. **7**, 1800589.

94. Qu, C., Xiao, Y., Zhou, H., et al. (2019). Quaternary ammonium salt based NIR-II probes for in vivo imaging. Adv. Opt. Mater. **7**, 1900229.

95. Li, D., Qu, C., Liu, Q., et al. (2019). Monitoring the real-time circulatory system-related physiological and pathological processes in vivo using a multifunctional NIR-II probe. Adv. Funct. Mater. **30**, 1906343.

96. Wan, H., Yue, J., Zhu, S., et al. (2018). A bright organic NIR-II nanofluorophore for three-dimensional imaging into biological tissues. Nat. Commun. **9**, 1171.

97. Zhang, L., Liu, C., Zhou, S., et al. (2019). Improving quantum yield of a NIR-II dye by phenylazo group. Adv. Healthc. Mater. **9**, 1901470.

98. Xiao, F., Lin, L., Chao, Z., et al. (2020). Organic spherical nucleic acids for the transport of a NIR-II-emitting dye across the blood-brain barrier. Angew. Chem. Int. Ed. **159**, 9702–9710.

99. Zhang, R., Xu, Y., Zhang, Y., et al. (2019). Rational design of a multifunctional molecular dye for dual-modal NIR-II/photoacoustic imaging and photothermal therapy. Chem. Sci. **10**, 8348–8353.

100. Zhang, H., Zhao, Z., Turley, A.T., et al. (2020). Aggregate science: from structures to properties. Adv. Mater. **32**, 2001457.

101. Liu, S., Li, Y., Kwok, R.T.K., et al. (2020). Structural and process controls of AIEgens for NIR-II theranostics. Chem. Sci. https://doi.org/10.1039/D0SC02911D.

102. Alifu, N., Zebibula, A., Qi, J., et al. (2018). Single-molecular near-infrared-II theranostic systems: ultrastable aggregation-induced emission nanoparticles for long-term tracing and efficient photothermal therapy. ACS Nano **12**, 11282–11293.

103. Sheng, Z., Guo, B., Hu, D., et al. (2019). Bright aggregation-induced-emission dots for targeted synergetic NIR-II fluorescence and NIR-I photoacoustic imaging of orthotopic brain tumors. Adv. Mater. **30**, 1800766.

104. Wu, W., Yang, Y.Q., Yang, Y., et al. (2019). An organic NIR-II nanofluorophore with aggregation-induced emission characteristics for in vivo fluorescence imaging. Int. J. Nanomedicine **14**, 3571–3582.

105. Xu, P., Kang, F., Yang, W., et al. (2020). Molecular engineering of a high quantum yield NIR-II molecular fluorophore with aggregation-induced emission (AIE) characteristics for in vivo imaging. Nanoscale **12**, 5084–5090.

106. Diao, S., Blackburn, J.L., Hong, G., et al. (2019). Fluorescence imaging in vivo at wavelengths beyond 1500 nm. Angew. Chem. Int. Ed. **54**, 14758–14762.

107. Li, Q., Ding, Q., Li, Y., et al. (2020). Novel small-molecule fluorophores for in vivo NIR-IIa and NIR-IIb imaging. Chem. Commun. **56**, 3289–3292.

108. Li, Y., Liu, Y., Li, Q., et al. (2019). Novel NIR-II organic fluorophores for bioimaging beyond 1550 nm. Chem. Sci. **11**, 2621–2626.

109. Li, Y., Cai, Z., Liu, S., et al. (2019). Design of AIEgens for near-infrared IIb imaging through structural modulation at molecular and morphological levels. Nat. Commun. **11**, 1255.

110. Zhang, R., Wang, Z., Xu, L., et al. (2019). Rational design of a multifunctional molecular dye with single dose and laser for efficiency NIR-II fluorescence/photoacoustic imaging guided photothermal therapy. Anal. Chem. **91**, 12476–12483.

111. Sun, Y., Ding, F., Zhou, Z., et al. (2019). Rhomboidal Pt(II) metallacycle-based NIR-II theranostic nanoprobe for tumor diagnosis and image-guided therapy. Proc. Natl. Acad. Sci. U S A **116**, 1968–1973.

112. Starosolski, Z., Bhavane, R., Ghaghada, K.B., et al. (2017). Indocyanine green fluorescence in second near-infrared (NIR-II) window. PLoS One **12**, 0187563.

113. Cai, Z., Zhu, L., Wang, M., et al. (2020). NIR-II fluorescence microscopic imaging of cortical vasculature in non-human primates. Theranostics **10**, 4265–4276.

114. Tian, R.A.O., Zeng, Q.A.O., Zhu, S.A.O., et al. (2019). Albumin-chaperoned cyanine dye yields superbright NIR-II fluorophore with enhanced pharmacokinetics. Sci. Adv. **5**, eaaw0672.

115. Zhu, S., Hu, Z., Tian, R., et al. (2018). Repurposing cyanine NIR-I dyes accelerates clinical translation of near-infrared-II (NIR-II) bioimaging. Adv. Mater. **30**, 4141–4151.

116. Feng, Z., Yu, X., Jiang, M., et al. (2019). Excretable IR-820 for in vivo NIR-II fluorescence cerebrovascular imaging and photothermal therapy of subcutaneous tumor. Theranostics **9**, 5706–5719.

117. Li, B., Zhao, M., and Zhang, F. (2020). Rational design of near-infrared-II organic molecular dyes for bioimaging and biosensing. ACS. Mater. Lett. **2**, 905–917.

118. Cosco, E.D., Caram, J.R., Bruns, O.T., et al. (2017). Flavylium polymethine fluorophores for near- and shortwave infrared imaging. Angew. Chem. Int. Ed. **56**, 13126–13129.

119. Ding, B., Xiao, Y., Zhou, H., et al. (2019). Polymethine thiopyrylium fluorophores with absorption beyond 1000 nm for biological imaging in the second near-infrared sub-window. J. Med. Chem. **62**, 2049–2059.

120. Li, B., Lu, L., Zhao, M., et al. (2018). An efficient 1064 nm NIR-II excitation fluorescent molecular dye for deep-tissue high-resolution dynamic bioimaging. Angew. Chem. Int. Ed. **57**, 7483–7487.

121. Sun, C., Li, B., Zhao, M., et al. (2019). J-aggregates of cyanine dye for NIR-II in vivo dynamic vascular imaging beyond 1500 nm. J. Am. Chem. Soc. **141**, 19221–19225.

122. Lei, Z., Sun, C., Pei, P., et al. (2019). Stable, wavelength-tunable fluorescent dyes in the NIR-II region for in vivo high-contrast bioimaging and multiplexed biosensing. Angew. Chem. Int. Ed. **58**, 8166–8171.

123. Wang, S., Fan, Y., Li, D., et al. (2019). Anti-quenching NIR-II molecular fluorophores for in vivo high-contrast imaging and pH sensing. Nat. Commun. **10**, 1058.

124. Chen, C., Tian, R., Zeng, Y., et al. (2020). Activatable fluorescence probes for "turn-on" and ratiometric biosensing and bioimaging: from NIR-I to NIR-II. Bioconjug. Chem. **31**, 276–292.

125. Li, D., Wang, S., Lei, Z., et al. (2019). Peroxynitrite activatable NIR-II fluorescent molecular probe for drug-induced hepatotoxicity monitoring. Anal. Chem. **91**, 4771–4779.

126. Feng, W., Zhang, Y., Li, Z., et al. (2019). Lighting up NIR-II fluorescence in vivo: an activable probe for noninvasive hydroxyl radical imaging. Anal. Chem. **91**, 15757–15762.

127. Tang, Y., Li, Y., Hu, X., et al. (2018). "Dual lock-and-key"-controlled nanoprobes for ultrahigh specific fluorescence imaging in the second near-infrared window. Adv. Mater. **30**, 1801140.

128. Li, T., Li, C., Ruan, Z., et al. (2019). Polypeptide-conjugated second near-infrared organic fluorophore for image-guided photothermal therapy. ACS Nano **13**, 3691–3702.

129. Zhao, M., Ding, J., Mao, Q., et al. (2020). A novel α$_v$β$_3$ integrin-targeted NIR-II nanoprobe for multimodal imaging-guided photothermal therapy of tumors in vivo. Nanoscale **12**, 6940–6958.

130. Boens, N., Verbelen, B., Ortiz, M.J., et al. (2019). Synthesis of BODIPY dyes through postfunctionalization of the boron dipyrromethene core. Coord. Chem. Rev. **399**, 213024.

131. Nguyen, V.N., Yim, Y., Kim, S., et al. (2020). Molecular design of highly efficient heavy-atom-free triplet BODIPY derivatives for photodynamic therapy and bioimaging. Angew. Chem. Int. Ed. **59**, 8957–8962.

132. Qi, S., Kwon, N., Yim, Y., et al. (2020). Fine-tuning the electronic structure of heavy-atom-free BODIPY photosensitizers for fluorescence imaging and mitochondria-targeted photodynamic therapy. Chem. Sci. **11**, 6479–6484.

133. Wang, Z., Huang, L., Yan, Y., et al. (2020). Elucidation of the intersystem crossing mechanism in a helical BODIPY for low-dose photodynamic therapy. Angew. Chem. Int. Ed. **59**, 16114.

134. Chen, D., Zhong, Z., Ma, Q., et al. (2020). Aza-BODIPY-based nanomedicines in cancer phototheranostics. ACS. Appl. Mater. Interfaces **12**, 26914–26925.

135. Bai, L., Sun, P., Liu, Y., et al. (2019). Novel aza-BODIPY based small molecular NIR-II fluorophores for in vivo imaging. Chem. Commun. **55**, 10920–10923.

136. Godard, A., Kalot, G., Pliquett, J., et al. (2020). Water-soluble aza-BODIPYs: biocompatible organic dyes for high contrast in vivo NIR-II imaging. Bioconjug. Chem. **31**, 1088–1092.

137. Xu, G., Yan, Q., Lv, X., et al. (2018). Imaging of colorectal cancers using activatable nanoprobes with second near-infrared window emission. Angew. Chem. Int. Ed. **57**, 3626.

138. Chen, J.A., Pan, H., Wang, Z., et al. (2020). Imaging of ovarian cancers using enzyme activatable probes with second near-infrared window emission. Chem. Commun. **56**, 2731–2734.

139. Dou, K., Huang, W., Xiang, Y., et al. (2020). Design of activatable NIR-II molecular probe for in vivo elucidation of disease-related viscosity variations. Anal. Chem. **92**, 4177–4181.

140. Liang, P., Tang, Q., Cai, Y., et al. (2017). Self-quenched ferrocenyl diketopyrrolopyrrole organic nanoparticles with amplifying photothermal effect for cancer therapy. Chem. Sci. **8**, 7457–7463.

141. Jiang, X., Wang, L., Tang, H., et al. (2020). Diketopyrrolopyrrole: an emerging phototherapy agent in fighting cancer. Dyes Pigm. **181**, 108599.

142. Wang, Q., Xia, B., Xu, J., et al. (2019). Biocompatible small organic molecule phototheranostics for NIR-II fluorescence/photoacoustic imaging and simultaneous photodynamic/photothermal combination therapy. Mater. Chem. Front. **3**, 650–655.

143. Wang, Q., Dai, Y., Xu, J., et al. (2019). All-in-one phototheranostics: single laser triggers NIR-II fluorescence/photoacoustic imaging guided photothermal/photodynamic/chemo combination therapy. Adv. Funct. Mater. **29**, 1901480.

144. Ilina, K., MacCuaig, W.M., Laramie, M., et al. (2020). Squaraine dyes: molecular design for different applications and remaining challenges. Bioconjug. Chem. **31**, 194–213.

145. Li, J., Lv, B., Yan, D., et al. (2015). Tunable self-assembled micro/nanostructures of carboxyl-functionalized squarylium cyanine for ammonia sensing. Adv. Funct. Mater. **25**, 7442–7449.

146. Shen, C.A., and Wurthner, F. (2020). NIR-emitting squaraine J-aggregate nanosheets. Chem. Commun. **56**, 9878–9881.

147. Sun, P., Wu, Q., Sun, X., et al. (2018). J-aggregate squaraine nanoparticles with bright NIR-II fluorescence for imaging guided photothermal therapy. Chem. Commun. **54**, 13395–13398.

148. Yao, D., Wang, Y., Zou, R., et al. (2020). Molecular engineered squaraine nanoprobe for NIR-II/photoacoustic imaging and photothermal therapy of metastatic breast cancer. ACS Appl. Mater. Interfaces **12**, 4276–4284.

149. Zhu, X., Liu, C., Hu, Z., et al. (2020). High brightness NIR-II nanofluorophores based on fused-ring acceptor molecules. Nano Res. **13**, 2570–2575.

150. Tang, C., Song, C., Wei, Z., et al. (2020). Polycyclic naphthalenediimide-based nanoparticles for NIR-II fluorescence imaging guided phototherapy. Sci. China Chem. **63**, 946–956.

151. Wang, Q., Xu, J., Geng, R., et al. (2020). High performance one-for-all phototheranostics: NIR-II fluorescence imaging guided mitochondria-targeting phototherapy with a single-dose injection and 808 nm laser irradiation. Biomaterials **231**, 119671.

152. Zhang, Z., Xu, W., Kang, M., et al. (2020). An all-round athlete on the track of phototheranostics: Subtly regulating the balance between radiative and nonradiative decays for multimodal imaging-guided synergistic therapy. Adv. Mater. **32**, 2003210.

153. Lavaud, L., Azarias, C., Canard, G., et al. (2020). Fused bis-azacalixphyrin that reaches NIR-II absorptions. Chem. Commun. **56**, 896–899.

154. Shao, W., Wei, Q., Wang, S., et al. (2020). Molecular engineering of D-A-D conjugated small molecule nanoparticles for high performance NIR-II photothermal therapy. Mater. Horiz. **7**, 1379–1386.

155. Pan, H., Li, S., Kan, J.L., et al. (2019). A cruciform phthalocyanine pentad-based NIR-II photothermal agent for highly efficient tumor ablation. Chem. Sci. **10**, 8246–8252.

156. Li, S., Deng, Q., Zhang, Y., et al. (2020). Rational design of conjugated small molecules for superior photothermal theranostics in the NIR-II biowindow. Adv. Mater. **32**, 2001146.

AUTHOR CONTRIBUTIONS

H.D., J.S., F.G., and X.D. contributed to the design and writing of this manuscript. Q.S. and W.W. gave suggestions of conceptual ideas and language improvements for the manuscript.

DECLARATION OF INTERESTS

The authors declare no competing interests.

LEAD CONTACT WEBSITES

http://iam.njtech.edu.cn/en/info/1022/1043.htm.